Clim Dyn (2016) 47:1049–1072
DOI 10.1007/s00382-015-2888-3

# Inhibition of mixed-layer deepening during winter in the northeastern Arabian Sea by the West India Coastal Current

**D. Shankar**[1,2] · **R. Remya**[1,2] · **P. N. Vinayachandran**[3] · **Abhisek Chatterjee**[4] · **Ambica Behera**[3]

Received: 17 March 2015 / Accepted: 20 October 2015 / Published online: 28 October 2015


**Abstract** Though the deep mixed layers (MLs) that form in the northeastern Arabian Sea (NEAS) during the winter monsoon (November–February) have been attributed to convective mixing driven by dry, cool northeasterly winds from the Indian subcontinent, data show that the deepest MLs occur in the northern NEAS and the maxima of latent-heat and net heat fluxes in the southern NEAS. We use an oceanic general circulation model to show that the deep MLs in the NEAS extend up to ~20°N till the end of December, but are restricted poleward of ~22°N (~23°N) in January (February). This progressive restriction of the deep mixed layers within the NEAS is due to poleward advection of water of lower salinity by the West India Coastal Current (WICC). The deep MLs are sustained till February in the northern NEAS because convective mixing deepens the ML before the waters of lower salinity reach this region and the wind stirring and convective overturning generate sufficient turbulent energy for the ML to maintain the depth attained in January. Though the atmospheric fluxes tend to cool the ML in the southern NEAS, this cooling is countered by the warming due to horizontal advection. Likewise, the cooling due to entrainment, which continues in the southern NEAS even as the ML shallows during January–February, is almost cancelled by the warming caused by a downwelling vertical velocity field. Therefore, the SST changes very little during December–February even as the ML shallows dramatically in the southern NEAS. These deep MLs of the NEAS also preclude a strong intraseasonal response to the intraseasonal variability in the fluxes. This role of horizontal advection implies that the ML depth in the NEAS is determined by an interplay of physical processes that are forced differently. The convective mixing depends on processes that are local to the region, but the advection is due to the WICC, whose seasonal cycle is primarily forced by remote winds. By inhibiting the formation of deep MLs in the southern NEAS, the WICC limits the region of formation of the high-salinity water masses of this region. Since the deep MLs in the NEAS have been linked to the high chlorophyll concentration there, our results imply that the conventional approach of averaging over boxes for studying the impact of physics on biogeochemistry can mask important details that are due to advection because it is the advective component of any budget that is most affected by the averaging process.

**Keywords** Mixed layer · Ocean dynamics · Turbulent mixing · Eastern boundary current · Indian Ocean · Chlorophyll · Monsoon · Biogeochemistry

✉ D. Shankar
shankar@nio.org

[1] CSIR-National Institute of Oceanography, Dona Paula, Goa 403004, India

[2] Academy of Scientific and Innovative Research (AcSIR), CSIR-National Institute of Oceanography, Dona Paula, Goa, India

[3] Indian Institute of Science, Bangalore, India

[4] ESSO-Indian National Centre for Ocean Information Services, Hyderabad, India

## 1 Introduction

The seasonally reversing winds over the north Indian Ocean (NIO; north of 5°S) drive a seasonally reversing circulation. This seasonality of the physical forcing leads to two phytoplankton growing seasons, one each during the summer monsoon (June–September; also called "southwest" monsoon) and winter monsoon (November–February; also

called "northeast" monsoon) Banse 1987. The link between the physical forcing and phytoplankton blooms has been the subject of several observational and modelling studies in the Arabian Sea, the western arm of the NIO (see, for example, Banse 1968, 1984, 1987; Madhupratap et al. 1996; McCreary et al. 1996, 2001, 2009; Wiggert et al. 2000, 2002, 2005, 2006, 2009; Lévy et al. 2007; Koné et al. 2009; Hood et al. 2009; Gomes et al. 2014). There exist significant regional differences, as noted by several authors, in the timing and extent of these blooms, but the importance of the physical forcing has been highlighted by all (Banse 1987; Naqvi 1991; Naqvi et al. 2006; Lévy et al. 2007; McCreary et al. 2009; Wiggert et al. 2009; Koné et al. 2009).

Observations and models show that in the eastern Arabian Sea (EAS) (Fig. 1), there is a difference in the phytoplankton blooms between the southern and northern parts (Fig. 2). Off the southern part of the Indian west coast, a bloom occurs only during the summer monsoon, when the mixed layer (ML) shallows as a consequence of upwelling; in contrast, the northeastern Arabian Sea (NEAS) shows two distinct blooms, one each during the summer and winter monsoons (Banse 1987; Lévy et al. 2007; McCreary et al. 2009; Koné et al. 2009). The summer bloom in the NEAS has also been attributed to upwelling (Banse 1968, 1987; Lévy et al. 2007; McCreary et al. 2009; Koné et al. 2009). The EAS is one of the three major upwelling regimes of the Arabian Sea, the other two occurring off Somalia and Oman (see, for example, Banse 1968, 1984; McCreary et al. 1993; Schott and McCreary 2001).

The productivity of the NEAS during winter was tentatively attributed initially to upwelling because of the

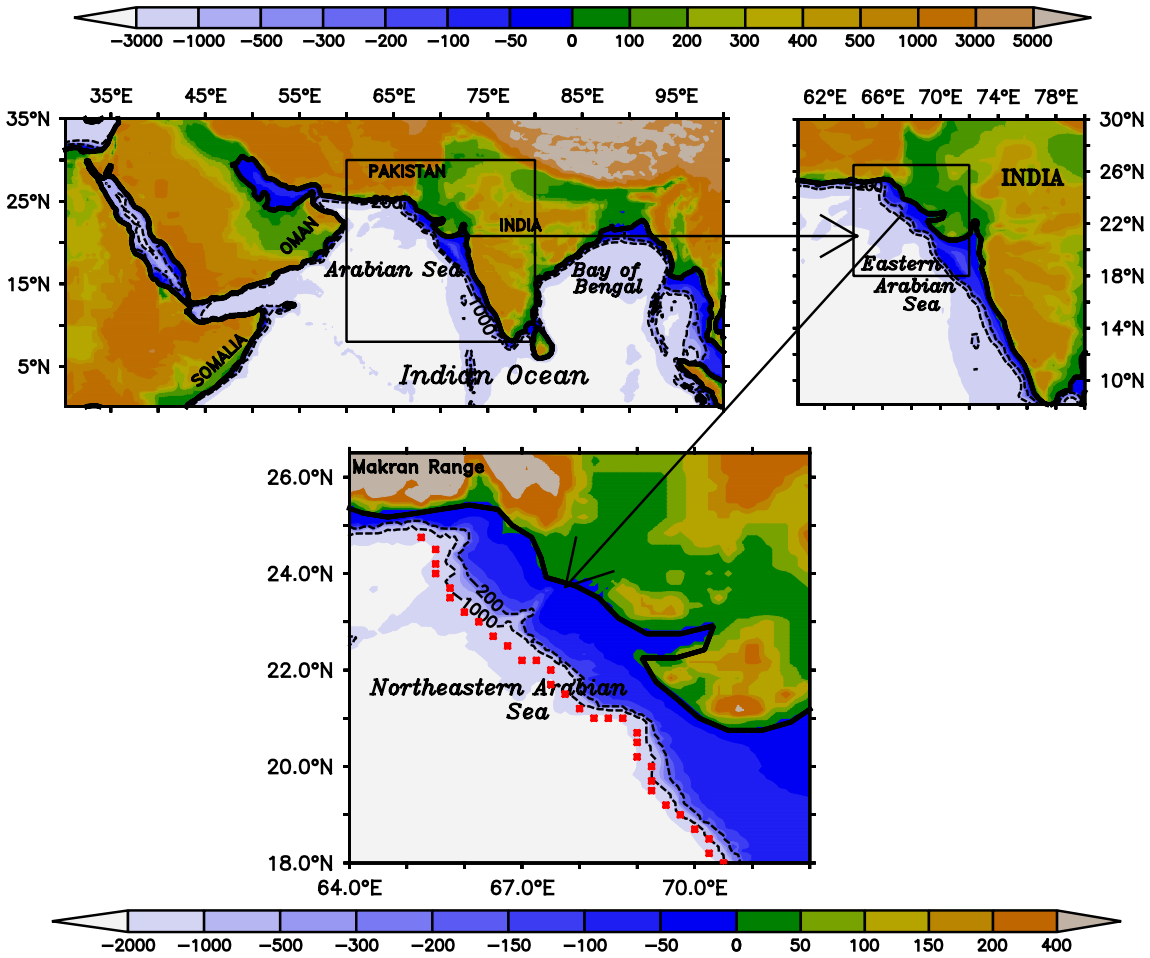


**Fig. 1** Map showing the region of interest. Ocean bathymetry (metres) and land topography (metres) are shown in all three panels. The shelf break is denoted by the 200 m isobath. Several figures in this paper show the variation in the NEAS along the 1000 m isobath, which is also shown; the model grid cells used for these figures are marked by filled *red squares*. The *top left panel* shows the large-scale map of the region of the region; the Arabian Sea is the western arm of the north Indian Ocean (NIO). The *box* marks the eastern Arabian Sea (EAS), which is shown in the *top right panel*. The topography in these two panels is based on the ETOPO20 data set. The *box* in the *top right panel* marks the northeastern Arabian Sea (NEAS), for which most of the spatial maps are plotted; the NEAS is shown in the *bottom panel*, which is based on the ETOPO5 data set as modified by Sindhu et al. (2007)

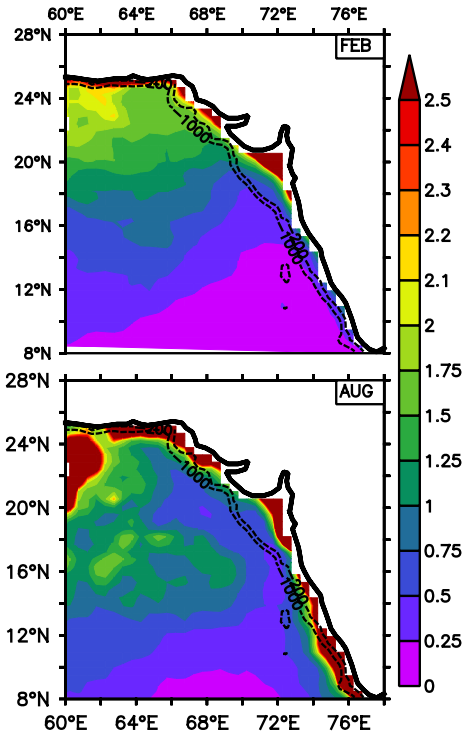


**Fig. 2** Climatological chlorophyll concentration (mg $m^{-3}$) in the EAS during February (*top*) and August (*bottom*); the data are from Lévy et al. (2006). Note that the colour scale is not uniform. There is no bloom in the southern EAS during February. The 200 and 1000 m isobaths are marked

existence of a cross-shore temperature gradient with the warmer waters occurring offshore (Carruthers et al. 1959), but Banse (1968) noted the absence of regular upwelling in the region during November–February. It is Banse (1968) who first pointed to the possibility of the lower sea surface temperatures (SSTs) observed in the NEAS during winter being a consequence of wind-driven surface cooling. The tide-gauge sea-level data in the EAS show a climatological maximum during winter (Banse 1984; Shetye and Almeida 1985), suggesting a poleward geostrophic boundary current that cannot favour upwelling during this season off the Indian west coast (Banse 1968, 1984; Sharma 1968; Pankajakshan and Ramaraju 1987; Shetye and Shenoi 1988). It was realised by this time that the large-scale boundary current in the EAS, the West India Coastal Current (WICC) (Shetye et al. 1990, 1991a; McCreary et al. 1993; Shankar and Shetye 1997; Shetye and Gouveia 1998; Schott and McCreary 2001; Shankar et al. 2002) flowed poleward into the local alongshore wind during winter (see Amol et al. 2014, for a brief history of the WICC literature), prompting Banse (1984) to suggest a role for the large-scale circulation in the forcing of the winter WICC.

All studies that we are aware of attribute the higher productivity and phytoplankton bloom in the NEAS during winter to this convective mixing that entrains nutrients into the surface ML as it deepens (Banse 1968, 1984, 1987; Madhupratap et al. 1996; Lévy et al. 2007; McCreary et al. 2009; Koné et al. 2009; Gomes et al. 2014), and available data suggest that this proposed link between the deep ML (Chatterjee et al. 2012) and the chlorophyll concentration (Lévy et al. 2006) is viable, with the higher chlorophyll concentration tending to be co-located with the deeper ML during winter (Fig. 3). The chlorophyll bloom peaks in February (Lévy et al. 2007), following the peak in the ML depth (MLD) (Fig. 3).

The dry, cool northeasterly winds blowing onto the sea from land are expected to cool the surface of the NEAS. All these studies (Banse 1968, 1984, 1987; Shetye et al. 1992; McCreary et al. 1993, 2009; Prasannakumar and Prasad 1996, 1999; Madhupratap et al. 1996; Lévy et al. 2007; Koné et al. 2009; Gomes et al. 2014) invoke the increase in latent-heat flux, a consequence of the northeasterly winds being both strong and dry, and the decrease in incoming shortwave flux during winter as the cause of the deep MLs. The increased evaporation is expected to lead to a decrease in surface temperature and an increase in the surface salinity and density, leading to convective mixing and the formation of one of the three high-salinity water masses of the NIO (Rochford 1964; Banse 1968, 1984; Wyrtki 1971; Shetye et al. 1992; Shenoi et al. 1993; Prasannakumar and Prasad 1999). This high-salinity water mass is characteristic of the northern Arabian Sea and has been called the Arabian Sea High-Salinity Water (ASHSW) mass (Rochford 1964). Modelling studies have validated this hypothesis of water-mass formation by deep convective mixing (McCreary et al. 1993; Han 1999; Han et al. 2001; Prasad and Ikeda 2002b, a; Lévy et al. 2007; Koné et al. 2009) and suggest that it forms over a broad region. The hydrographic data show that salinity decreases below the ML (Rochford 1964; Wyrtki 1971; Varma et al. 1980; Shetye et al. 1992; Shenoi et al. 1993); this intermediate layer of lower salinity, which would imply an unstable water column if it were not for a sharp decrease in temperature at the base of the ML to counter the haline effect, has been called the Arabian Sea Salinity Minimum (Shenoi et al. 1993).

While all these studies invoke deep convective mixing as the cause of the deep MLs, their spatial focus has been constrained by the availability of data. Much of the literature even for the northern Arabian Sea is therefore restricted to the region sampled by the international and Indian JGOFS (Joint Global Ocean Flux Study) programmes of the mid-1990s (Prasannakumar and Prasad 1996; Madhupratap et al. 1996; Wiggert et al. 2000, 2002, 2005). None of these JGOFS cruises sampled the region of deep MLs in the northernmost Arabian Sea (Fig. 3), for which most of the data available are from the International Indian Ocean Expedition (IIOE) of the 1960s (Wyrtki 1971; Levitus

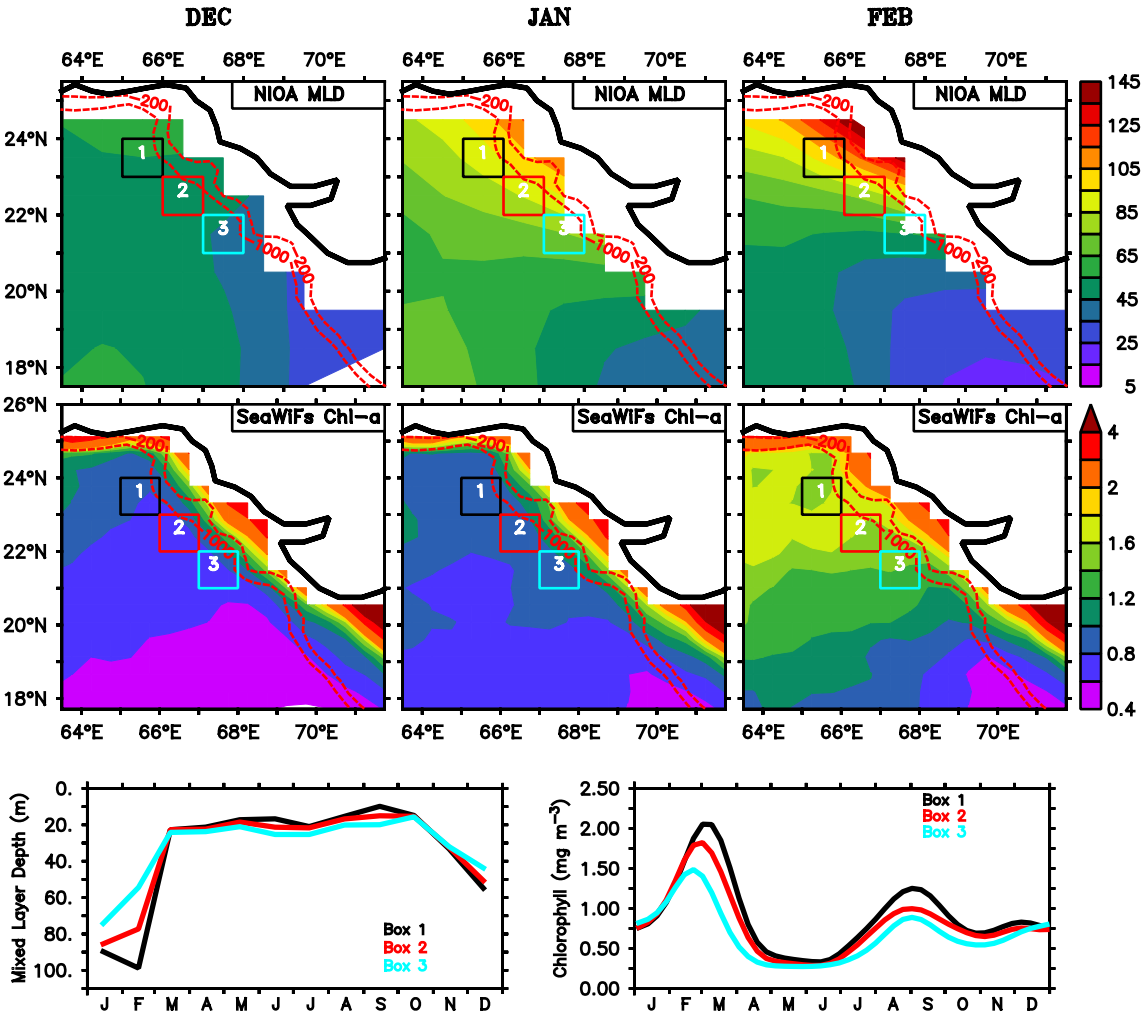


**Fig. 3** Observed monthly climatologies of MLD (metres; *top panels*), based on the monthly temperature and salinity climatologies of Chatterjee et al. (2012) (NIOA: North Indian Ocean Atlas), and chlorophyll concentration (mg $m^{-3}$; *middle panels*), based on the weekly climatology of Lévy et al. (2006), in the NEAS during December–February (*left* to *right*). Note that the colour scale for chlorophyll is not uniform. The 200 and 1000 m isobaths are marked. The two panels in the *bottom row* show the annual cycle of MLD (*left*) and chlorophyll concentration (*right*) for the *three boxes* marked in the contour maps. Both MLD and chlorophyll concentration increase from south to north during the winter monsoon (November–February)

1982; Locarnini et al. 2010; Antonov et al. 2010; Chatterjee et al. 2012) and two cruises during the 1970s (Varma et al. 1980; Banse and Postel 2009). The more recent data are largely due to Argo floats and an examination of the distribution of hydrographic profiles shows an extremely sparse distribution of data in the northern NEAS (see Figures 1, 20, and 21 in Chatterjee et al. 2012), which accounts for the deepest mixed layers. The ASHSW forming in this region sinks to a depth greater than does the ASHSW formed farther south in the NEAS (Naqvi et al. 2006) and was therefore distinguished as the Northern Arabian Sea High-Salinity Water (NASHSW) mass by Banse and Postel (2009).

Curiously, however, observations show that the regimes of the deepest MLs (Varma et al. 1980; Banse and Postel 2009; Chatterjee et al. 2012) and the highest latent-heat flux (Praveenkumar et al. 2012) do not coincide (Fig. 4): the deepest MLs are in the northernmost part of the NEAS, where the NASHSW forms, but the highest latent-heat flux occurs farther to the south, where the winds are stronger, but the ML is thinner and the water mass that forms is the ASHSW. The sensible-heat flux [all fluxes in Fig. 4 are from Praveenkumar et al. (2012)] is higher in the north, but this flux is almost an order of magnitude smaller than the latent-heat flux. The net longwave flux varies more cross-shore than alongshore. The net shortwave flux into the ocean is less in the northern NEAS, complementing the latent-heat flux, but the net flux out of the ocean during January is still higher in the southern NEAS. A similar discrepancy between the fluxes and deep MLs is seen during February.

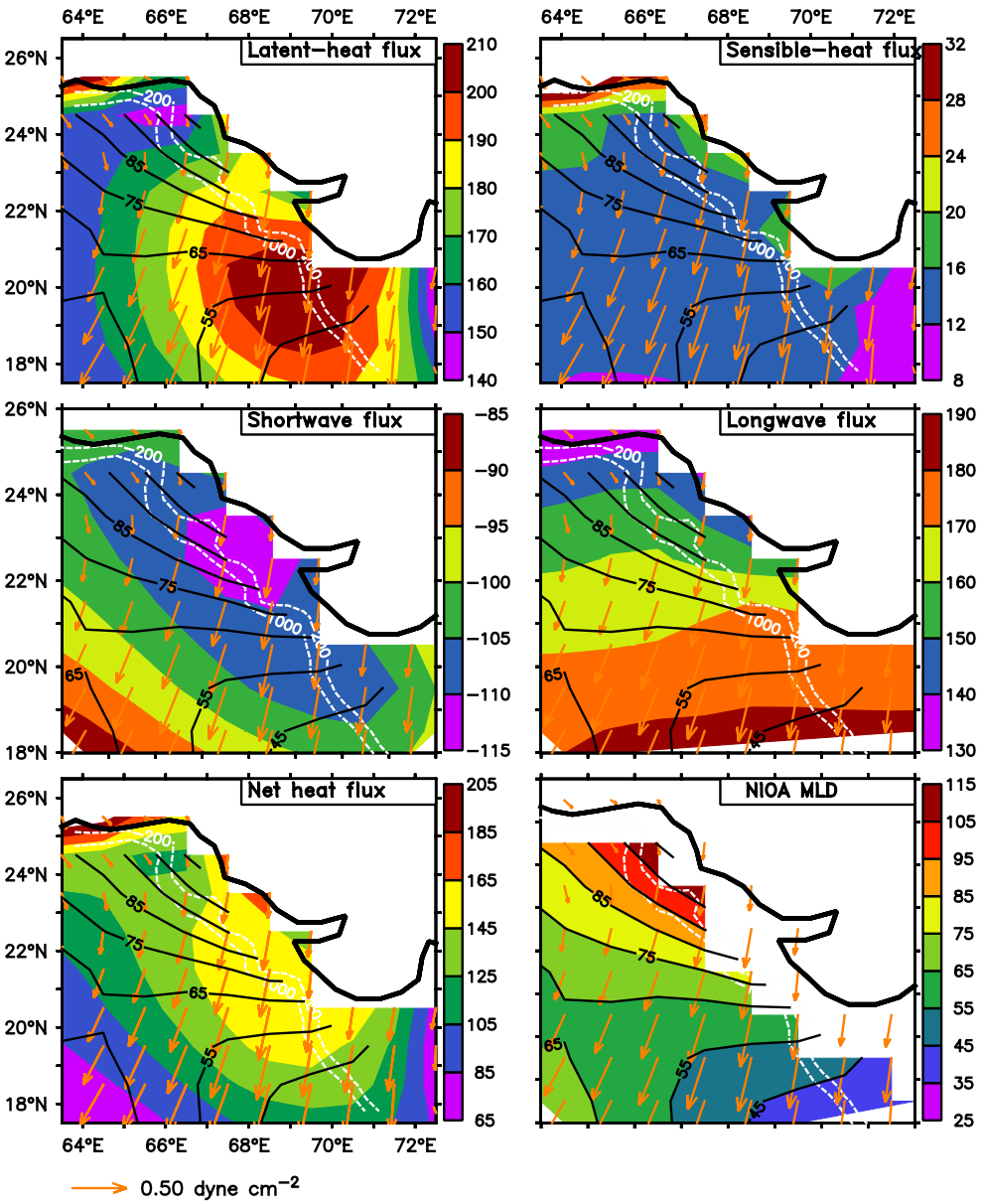


**Fig. 4** Climatological monthly latent heat flux (*top left*), sensible heat flux (*top right*), net shortwave flux (*middle left*), net longwave flux (*middle right*), and net heat flux (*bottom left*) during January in the NEAS. Superimposed on these five maps are the MLD contours (metres) for January; the MLD for January is plotted in the *bottom right panel*. All the fluxes are in W m$^{-2}$, with positive values implying a flux out of the ocean; note that the colour scale is different for each panel. The flux climatologies were computed using data for 1979–2013. Superimposed on the flux and MLD maps are the wind-stress vectors (dyne cm$^{-2}$). The wind stress and fluxes are from Praveenkumar et al. (2012) and the MLD is based on Chatterjee et al. (2012). The 200 and 1000 m isobaths are marked

That the deepest MLs do not coincide with the highest latent-heat flux and that the spatial differences in MLD are not matched by similar gradients in the net flux out of the ocean suggests that processes other than convective mixing driven by local winds are also important. Though Naqvi et al. (2006) state that "the lower salinity and higher temperature of the water derived from the south do not permit sufficient densification to trigger convective mixing, except in the most northern parts", a quantitative study of the impact of advection has not been carried out. The simulations of Han et al. (2001) suggest that evaporation affects the MLD in the NEAS and that the effect is not uniform in space, but their study dealt with the entire Indian Ocean and therefore did not quantify the processes specifically for the NEAS.

In this paper, we use an oceanic general circulation model (OGCM) to investigate the factors that determine the MLD during winter in the NEAS, which we define as

**Table 1** Model physics, including coordinate systems and parameterisations used

| Physics | Remarks | References/source |
|---|---|---|
| Coordinate system | Generalised orthogonal coordinates horizontally and quasi-horizontal, rescaled height coordinate vertically | Stacey et al. (1995)<br>Adcroft and Campin (2004) |
| Bottom topography | Modified ETOPO2 bathymetry | Sindhu et al. (2007) |
| Initial temperature and salinity fields (also used for relaxation at open boundaries) | Adds data from the Indian EEZ (Exclusive Economic Zone) to the World Ocean Atlas of Locarnini et al. (2010) and Antonov et al. (2010) | Chatterjee et al. (2012) |
| Equation of state | Nonlinear formulation | Jackett et al. (2006) |
| Tracer advection | Multi-dimensional, piecewise parabolic method (MDPPM) | http://mitgcm.org/ |
| Vertical mixing | *K*-profile parameterisation, with a pre-specified vertical-diffusivity profile (Bryan and Lewis 1979) and a critical bulk Richardson number of 0.3 (local mixing due to double diffusion not included to avoid enhanced mixing within the stratified water column) | Large et al. (1994) |
| Horizontal friction | Combination of biharmonic and Laplacian mixing, with Smagorinsky mixing coefficients of 0.01 (velocity scale 0.04 m $s^{-1}$) and 0.1 (velocity scale 0.005 m $s^{-1}$), respectively | Griffies and Hallberg (2000) |
| Penetrative shortwave heating | In upper 100 m, calculated using a Chl-*a* based scheme | Morel and Antoine (1994) |

the region east of 64°E and north of 18°N (Fig. 1). Though the high chlorophyll concentration in the NEAS provides the motivation for this study, our focus in this paper is restricted to the physical processes determining the spatio-temporal variation of MLD within the NEAS during the winter monsoon. We show that the deep MLs in the NEAS extend up to ~20°N till the end of December, but are restricted poleward of ~22°N (~23°N) in January (February). This progressive restriction of the deep mixed layers within the NEAS is due to poleward advection of water of lower salinity by the boundary current, the WICC. We also show that the decrease in MLD in the southern NEAS, particularly large in February, is not matched by a corresponding change in the SST. The paper is organised as follows. In Sect. 2, we present the model details. The evolution of the model ML in the NEAS during winter is presented in Sect. 3 and the role of advection is analysed in Sect. 4. Section 5 concludes the paper.

## 2 The model

Our OGCM is version MOM4p1 of MOM (Modular Ocean Model) (Griffies 2009), configured for the Indian Ocean as in Kurian and Vinayachandran (2007), Vinayachandran et al. (2007), and Chatterjee et al. (2013). A detailed description of the model setup is given in Chatterjee et al. (2013) and we provide but an overview here.

MOM has a free surface and uses the hydrostatic approximation. The horizontal resolution in our setup is 0.25° × 0.25° and there are 40 vertical levels, with 25 levels in the top 200 m and a 5-m resolution in the top 60 m. The model domain extends over the Indian Ocean (30° –120°E, 30°S–30°N). Bottom topography is based on a modified ETOPO2 bathymetry (Sindhu et al. 2007), with the minimum ocean depth set to 15 m and isolated land points (i. e., single cells) removed. The Palk Strait between India and Sri Lanka is closed, and the outflow regions of the Red Sea and Persian Gulf are broadened and deepened to ensure smooth flow between these narrow channels and the Arabian Sea. At land boundaries, a no-flux condition is imposed for tracers and no-slip and no-normal-flow conditions are imposed for velocity. Sponge layers of width 3.5° are applied to the open southern (30°S) and eastern (120°E) boundaries, where tracer fields are relaxed to climatological values (Chatterjee et al. 2012) with a time scale of 30 days; no restoration is applied to the tracer fields elsewhere in the model domain. The Chatterjee et al. (2012) climatology adds data within the Indian Exclusive Economic Zone (EEZ) from Indian sources to the data set that was used to prepare the temperature and salinity climatologies of the World Ocean Atlas (Locarnini et al. 2010; Antonov et al. 2010); inclusion of these Indian data leads to significant improvement in the climatology within the Indian EEZ by presenting more stable climatological values. The model physics and parameterisation choices are listed in Table 1.

Sources for the model forcing are listed in Table 2. River discharge, based on the data set of Vörösmarty et al. (1996), is specified in the top two layers of the vertical grid; the discharge for the Ganga and Brahmaputra, which have the highest discharge into the NIO, is, however, based on the more recent data set from Papa et al. (2010). Most of the forcing is from the OMIP (Ocean Model Inter-comparison Project) (Röske 2001) data set. The OMIP data, which constitute a daily climatology, are derived from ECMWF (European Centre for Medium-range Weather Forecasting)

**Table 2** List of data sets used to force the MOM4p1 model

| Field (units) | Data source | Frequency | References |
|---|---|---|---|
| Wind stress ($N\,m^{-2}$) | OMIP | Daily | Röske (2001) |
| Wind speed ($m\,s^{-1}$) | OMIP | Daily | Röske (2001) |
| Downward shortwave radiation ($W\,m^{-2}$) | OMIP | Daily | Röske (2001) |
| Downward longwave radiation ($W\,m^{-2}$) | OMIP | Daily | Röske (2001) |
| Air temperature (K) | OMIP | Daily | Röske (2001) |
| Specific humidity ($kg\,kg^{-1}$) | OMIP | Daily | Röske (2001) |
| Precipitation ($m\,s^{-1}$) | CMAP | Daily | Xie and Arkin (1997) |
| River runoff ($m\,s^{-1}$) | SAGE (UNESCO) | Monthly | Vörösmarty et al. (1996) Papa et al. (2010) |
| Chlorophyll ($mg\,m^{-3}$) | SeaWiFS | Monthly | Sweeney et al. (2005) |

From left to right, the table columns list the data type, source, frequency, and a reference that describes the data

Reanalysis for 1979–1993 (Gibson et al. 1997) and provide a consistent forcing set that has been used for inter-comparison of model forecasts. The model ocean was spun up from a state of rest for 14 years and the results presented are for the 15th year.

The model simulation has been validated earlier for the NIO (Kurian and Vinayachandran 2007; Vinayachandran et al. 2007) and equatorial IO (Chatterjee et al. 2013) and we restrict our model validation to monthly climatologies of MLD, SST, and sea-surface salinity (SSS). (Unless otherwise stated, SST and SSS refer to the temperature and salinity, respectively, of the ML.) Climatological observed MLD is calculated from the Chatterjee et al. (2012) data set using a density criterion: the MLD is defined as the depth at which the density increase from the surface surface corresponds to a 0.5 °C decrease in temperature (Shenoi et al. 2004). The model MLD is defined as the depth at which the buoyancy difference with respect to the surface level is equal to 0.0003 $m\,s^{-2}$ (Kurian and Vinayachandran 2007). (Computing the model MLD with the criterion used by Chatterjee et al. (2012) leads to a difference of but a few metres, which is inconsequential for the results of this paper. Hence, we stick to the more commonly used MLD criterion for MOM.)

The model simulation compares well with the observations (Fig. 5). As noted by Kurian and Vinayachandran (2007), the model WICC matches that observed (Mariano et al. 1995). For validating SST, we compare the model simulation with TMI (TRMM Microwave Imager; TRMM: Tropical Rainfall Measuring Mission). The model SST is within 0.5 °C of the observations throughout the year over the model domain even without flux correction (Kurian and Vinayachandran 2007), but the model is cooler in the NEAS throughout the winter monsoon. For salinity, the only data set available is based on hydrography and one must remember that the salinity data are extremely sparse in the NEAS (Chatterjee et al. 2012). The model simulates a lower salinity than observed, but the alongshore salinity variation, important for this analysis, is simulated fairly well. Without any artificial methods like salinity relaxation, the southeastern Arabian Sea (SEAS) freshens at the same time as in the observations and the poleward advection of low-salinity waters off the Indian west coast is more striking than in the observations (Kurian and Vinayachandran 2007). This role of advection in determining the spatial variation of SSS is evident in the model, whose finer resolution (0.25° × 0.25° compared to 1° × 1° for the observed climatology) makes it possible to see clearly the low-salinity tongue, due to the WICC, separating the higher-salinity waters on the shelf from the higher-salinity waters offshore of the WICC (Fig. 5). In the NEAS, the model simulates a deeper ML than observed and the deep MLs extend farther south in the model than in the observations, but the spatio-temporal variation of MLD within the NEAS is evident in both observations and model. The correlations between the modelled and observed MLD, SST, and SSS for the NEAS are 0.78, 0.92, and 0.65, respectively (0.83, 0.89, and 0.64, respectively) during October–March (full year); all these correlations are significant at the 99 % level. (The SST correlations are for the model and TMI; the MLD and SSS correlations are for the model and the climatology of Chatterjee et al. (2012).

## 3 Evolution of the mixed layer in the NEAS during winter

### 3.1 Evolution of the mixed layer and air-sea fluxes

The annual range of SST (model ML temperature) in the NEAS is ∼6 °C. SST falls below 26.5 °C in the northern NEAS (north of 23°N) during November and the 26 °C contour extends equatorward to 19.5°N along the continental slope (marked by the 1000 m isobath) in December (Fig. 5). SST decreases inshore and the coolest waters are near the coast, as noted earlier (Carruthers et al. 1959). SST

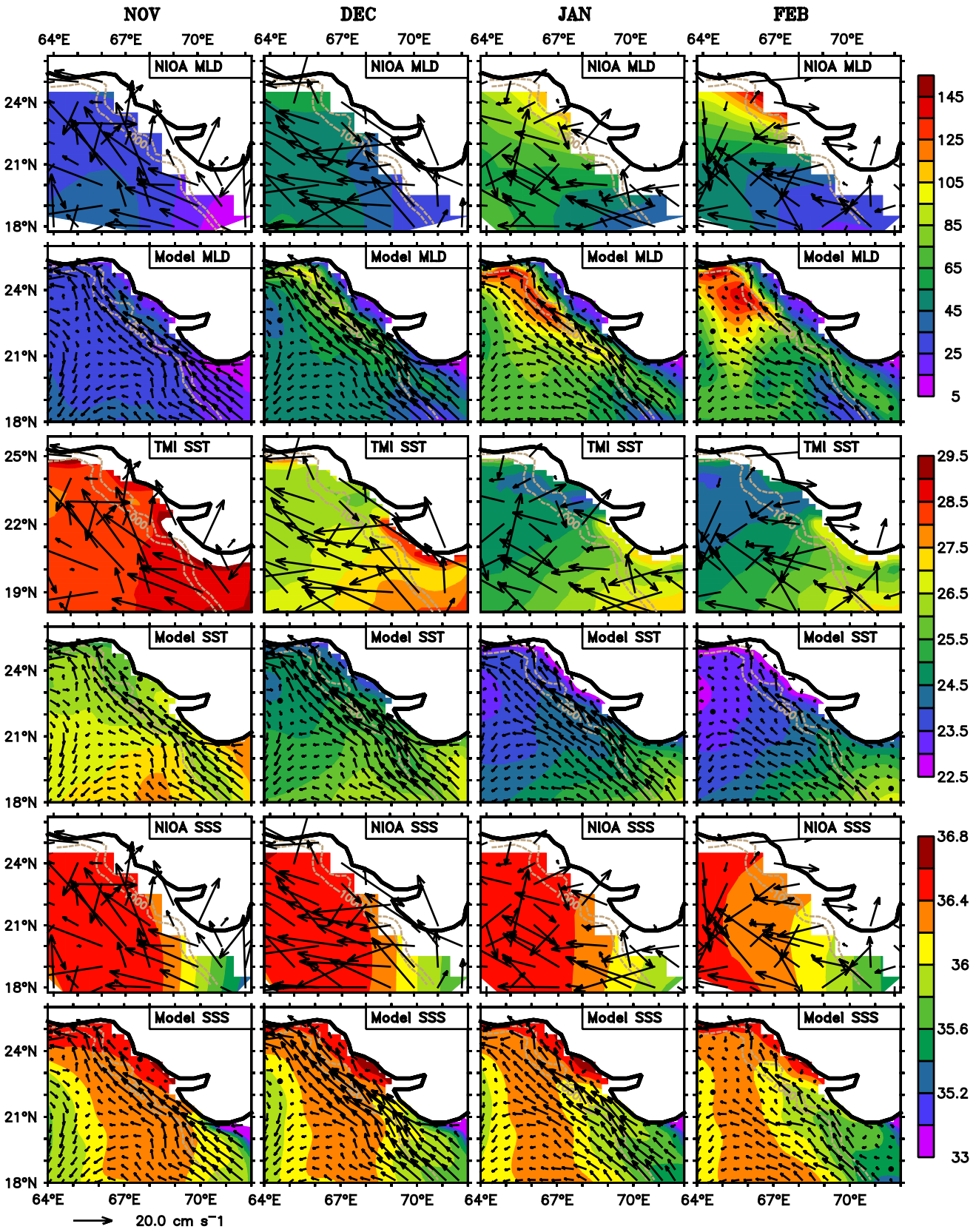
NOV
DEC
JAN
FEB
64°E
67°E
70°E
NIOA MLD
Model MLD
TMI SST
Model SST
NIOA SSS
Model SSS
24°N
21°N
18°N
25°N
22°N
19°N
145
125
105
85
65
45
25
5
29.5
28.5
27.5
26.5
25.5
24.5
23.5
22.5
36.8
36.4
36
35.6
35.2
33
20.0 cm s⁻1

◀ **Fig. 5** Monthly climatologies of observed MLD (*first row*), model MLD (*second row*), observed SST (*third row*), model SST (*fourth row*), observed SSS (*fifth row*), and model SSS (*sixth row*) during November–February (from *left* to *right*) for the NEAS. The units are metres for MLD, °C for SST, and psu (practical salinity unit) for SSS. The SST climatology is based on TMI data for 2000–2008 (ftp://ftp.ssmi.com/tmi/bmaps_v04/) and the SSS and MLD climatologies are based on Chatterjee et al. (2012). Overlaid on all panels are the surface currents (cm $s^{-1}$). The observed currents, overlaid in the observation panels, are from Mariano et al. (1995); the model surface currents are overlaid in the model panels. The 200 and 1000 m isobaths are marked

decreases in the NEAS till February, but the difference at 22°N from December–February is just ∼1.5 °C. The warming of the NEAS starts in March.

SSS (model ML salinity) is expected to increase during winter as a consequence of the evaporative cooling, but remains almost constant during October–November. SSS remains practically constant—its value hovers around 36.4 psu (practical salinity unit)—during November–January in the north and offshore, away from the regime of the narrow WICC (Fig. 5). Farther south, however, SSS at 22°N on the 1000 m isobath decreases from 36.3 to 35.9 psu from November to February.

The model ML starts deepening after October, but the MLD in the NEAS on the continental slope is still of the order of 30 m in November. It is during this transition period that the WICC reverses direction (Shetye and Shenoi 1988; McCreary et al. 1993; Shetye and Gouveia 1998; Schott and McCreary 2001) (Fig. 5). In December, the ML deepens beyond 80 m in patches on the continental shelf and deepens to ∼90 m on the continental slope (just offshore of the 1000 m isobath); the deepening of the ML in December is almost uniform all along the continental slope poleward of ~20°N (Fig. 5). In this regime of the NEAS, the ML continues to deepen through January, but the deepening is much greater north of ~22°N (∼140 m) than between 20 and 22°N (∼90 m). In February, the ML shallows in the southern NEAS to ∼60 m and the regime of shallow MLs extends up to ~23°N; poleward of ~23°N, the region of deep MLs extends farther offshore than in January. In March (figure not shown), the ML shallows all over the NEAS.

Though the deeper MLs occur north of 22–23°N (Fig. 5), the net heat flux out of the ocean is less north of 23°N (Fig. 6), implying weaker convective mixing. As may be expected, the longwave and sensible-heat fluxes do not vary significantly with latitude in the NEAS, and the north-south difference in net heat flux is essentially determined by the latent-heat and shortwave fluxes (Fig. 6). Throughout this paper, positive values imply fluxes out of the ocean. Though the shortwave flux into the ocean decreases poleward, the latent-heat flux is less poleward of ∼23°N, i.e., in the northern NEAS, during December–January. As a consequence of this distribution of the air-sea fluxes on the continental slope, the net heat flux during December is ∼20 W $m^2$ higher at 21°N compared to 24°N, implying stronger convective mixing in the southern NEAS. In February, the shortwave flux increases all over the NEAS, but the difference in net heat flux between the northern and southern NEAS changes sign, with the outgoing flux at 24°N exceeding that at 21°N by ∼20 W $m^2$.

### 3.2 The questions

The evolution of the ML during winter in the NEAS leads to three questions. First, substantial deepening of the ML is highly localised even within the NEAS and does not coincide with the high latent-heat or net heat fluxes out of the ocean. Therefore, the question is why the ML shallows in the southern NEAS even as it continues to deepen in the north after December? The second question is a corollary of the first question: what sustains the deep ML in the northern NEAS during February? Third, even as the MLD undergoes large changes in the southern NEAS during January–February, the SST barely changes. Naqvi et al. (2006) suggested that the relatively shallower ML in the southern NEAS is due to the poleward advection of fresher and warmer water by the WICC. Since the SST does increase from north to south (Fig. 5), implying that the WICC will advect warmer waters poleward, and the net heat flux out of the ocean decreases all over the NEAS from January to February (Fig. 6), why does the SST not increase at least in the southern NEAS? The analysis carried out in the rest of this paper is aimed at answering these three questions. We begin by analysing the contribution of the winds (momentum fluxes) and buoyancy fluxes to the spatio-temporal variation in the MLD.

### 3.3 Mixed-layer physics

When the ML shallows, the Monin–Obukhov depth (Monin and Obukhov 1954) is often used to describe the balance between the turbulent kinetic energy (TKE) input by the momentum fluxes due to the wind and the buoyancy fluxes in the ML. The idea is that if the TKE input by the wind is not sufficient to maintain the MLD when the buoyancy fluxes are negative (equivalent to a heat gain at the ocean surface according to the sign convention used in this paper), then the ML shallows to the Monin–Obukhov depth, $H_{\mathrm{MO}}$ (Kraus and Turner 1967; Qiu and Kelly 1993; McCreary et al. 1996; Han et al. 2001; Rao et al. 2002). Production of TKE is given by (following Han et al. 2001; Rao et al. 2002)

$$P_{\mathrm{TKE}} = \rho u_*^3 + \rho \kappa H_{\mathrm{MO}} B_0, \tag{1}$$

where $\rho$ is the density of sea water (1026 kg $m^{-3}$), $\kappa = 0.42$ is the von Kärmän constant (Rao et al. 2002), $u_* = \sqrt{\frac{\tau}{\rho}}$ is the friction velocity (with $\tau$ the magnitude of the wind stress), $g$ is the acceleration due to gravity, and

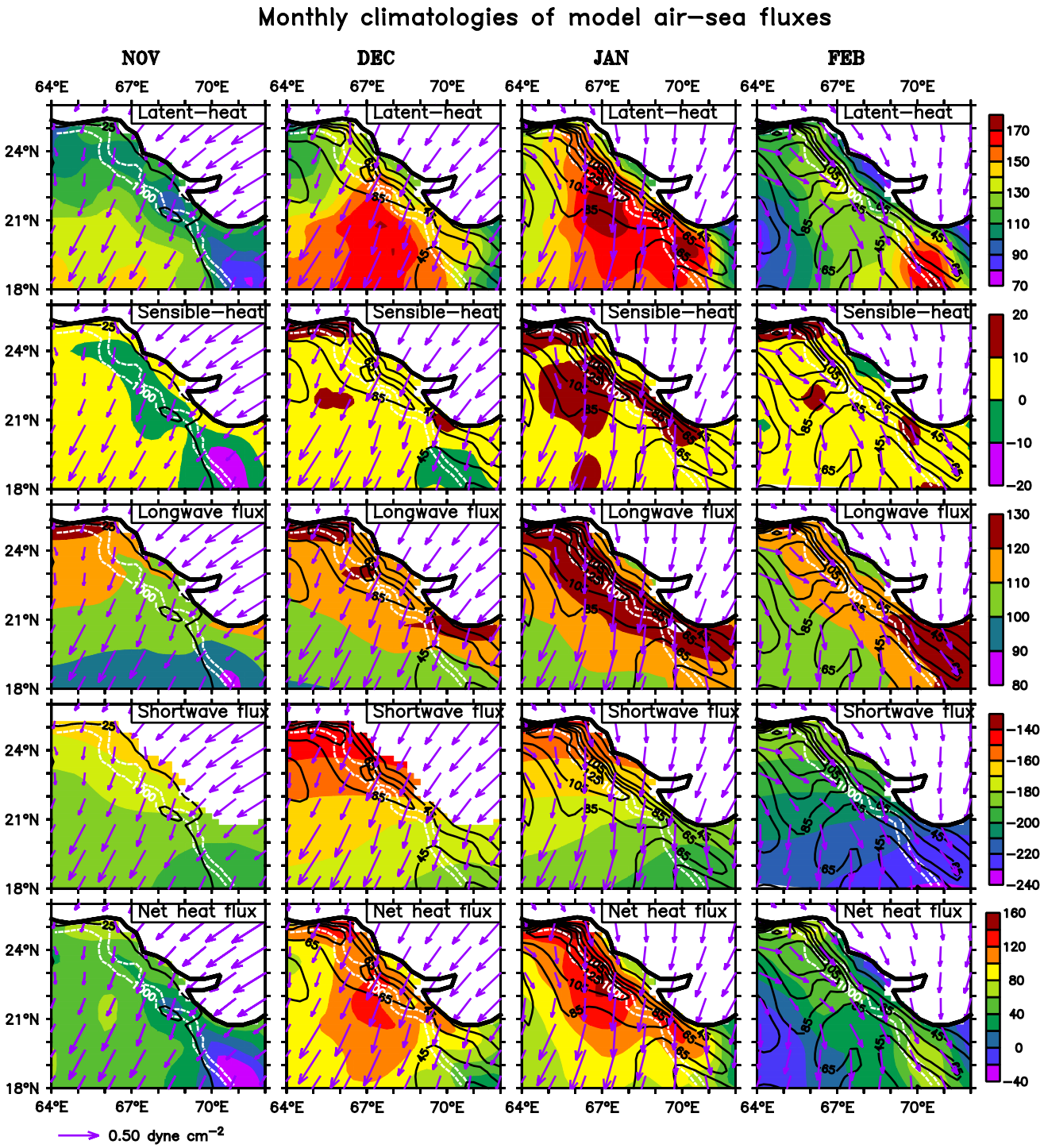


**Fig. 6** Monthly climatologies of the model air-sea flux fields. The daily model fluxes were averaged over the month to obtain these monthly climatologies and the sign convention is that a positive value indicates flux out of the ocean. The variables plotted for November–February (from *left* to *right*) are latent-heat flux (*first row*), sensible-heat flux (*second row*), net longwave flux (*third row*), net shortwave flux (*fourth row*), and net heat flux (*fifth row*). The model MLD and OMIP wind-stress vectors are superimposed on all the maps; the contour interval for MLD is 20 m. The units are W m$^{-2}$ for the fluxes, metres for MLD, and dyne cm$^{-2}$ for the wind stress. The 200 and 1000 m isobaths are marked

$$B_0 = 0.5g\left[-\frac{\alpha Q_0}{\rho C_p} + \beta(E-P)S_0\right] \quad (2)$$

is the depth-averaged buoyancy flux (unit m$^2$ s$^{-3}$) (Han et al. 2001; Cronin and Sprintall 2001). Note that the buoyancy flux of the ML is given by $B_0 H$, where $H$ is the MLD.

In Eq. (2), $C_p$ is the specific heat constant (at constant pressure) for sea water, $Q_0$ is the net heat flux out of the marine boundary layer (positive out of the ocean, so that a positive $Q_0$ will tend to deepen the ML), $E$ is the evaporation rate, $P$ is the precipitation rate, $S_0$ is the salinity of the ML, and $\alpha = -0.00025\ \mathrm{K}^{-1}$ and $\beta = 0.00785\ \mathrm{psu}^{-1}$ are the thermal expansion coefficient and haline contraction coefficient, respectively. Note that $Q_0 = Q_{\mathrm{net}} - Q_d$, where $Q_{\mathrm{net}}$ is the net heat flux at the ocean surface and $Q_d$ is the shortwave heat flux lost at the bottom of the mixed layer (the penetrative heat flux), and that this description of the heat budget does not include advection, which, as we shall see, makes a significant contribution to the heat budget of the ML in the NEAS.

The first term on the RHS of Eq. (1) represents the production of TKE by wind stirring and the second term the sum of thermal and haline buoyancy fluxes. The wind-stirring term, by definition, cannot be negative; hence, a balance between the two terms, leading to $P_{\mathrm{TKE}} = 0$ and a physically realistic or positive $H_{\mathrm{MO}}$, is possible only when the buoyancy flux is negative, implying a net heat gain by the ocean and/or an excess of precipitation over evaporation. When this balance holds,

$$H_{\mathrm{MO}} = -\frac{u_*^3}{\kappa B_0}. \tag{3}$$

In the NEAS, evaporation exceeds precipitation throughout the winter monsoon, implying a positive buoyancy flux due to the haline component. Therefore, a change of sign in the buoyancy flux can only come from the thermal buoyancy component. The thermal buoyancy flux in this region is an order of magnitude greater than the term representing turbulent energy generated by the winds (Fig. 7). The shallowing of the ML from February to March is due to a negative thermal buoyancy flux, a consequence of the increase in solar radiation leading to a net heat flux into the ocean. This negative thermal buoyancy flux overwhelms the smaller haline buoyancy flux, leading to a physically sensible, i. e., positive, $H_{\mathrm{MO}}$ at the end of the winter monsoon.

In contrast, the shallowing of the ML in the southern NEAS from January to February is not associated with a negative thermal buoyancy flux (Fig. 7). Indeed, the net heat flux is out of the ocean over almost the entire NEAS during February (Fig. 6), leading to a positive thermal buoyancy flux. Therefore, the buoyancy flux (Fig. 7) supports convective overturning throughout the winter monsoon and implies a negative (physically meaningless) $H_{\mathrm{MO}}$. Comparison of the pattern of MLD and buoyancy fluxes (thermal, haline, and total) during January–February shows an almost perfect match, suggesting a close relation between the two variables. Since the buoyancy fluxes include MLD [i. e., the buoyancy flux is the product of $B_0$ and the MLD in Eq. (1)], this match is not surprising. A plot of the depth-averaged buoyancy fluxes (i. e., $B_0$) shows that the spatial scale over which these quantities (or even the surface buoyancy fluxes) vary is much larger (Fig. 8), as may be expected from the similar spatial scales for the net heat flux from January to February (Fig. 6).

This striking difference between the large-scale changes in the depth-averaged buoyancy fluxes and the much more slope-trapped pattern of the buoyancy fluxes implies that there is more to the spatial and temporal variation of the MLD in the NEAS than merely the convective mixing invoked in the literature. The wedge-shaped intrusion, from south to north, of fresher water along the continental slope separates waters of higher salinity on the shelf and farther offshore of this wedge created by the WICC (Fig. 5); this role of the WICC has been suggested earlier (Prasannakumar and Prasad 1999; Han et al. 2001; Naqvi et al. 2006), and we analyse it in the following section.

## 4 Role of advection

To quantify the role of advection, it is necessary to recognise that the WICC hugs the continental slope (Shetye et al. 1991a) (Fig. 5). This boundary current propagates offshore as a Rossby wave on seasonal time scales (McCreary et al. 1993; Shankar and Shetye 1997; Shankar et al. 2002, 2010), but it narrows poleward (Shetye et al. 1991a) because the phase speed of the westward propagating Rossby wave decreases as the square of the distance from the equator. Even at 10°N, the theoretical and observed Rossby-wave speed for the first baroclinic mode is ∼10 cm $\mathrm{s}^{-1}$ (Shankar et al. 2004), implying a speed of ∼2 cm $\mathrm{s}^{-1}$ in the NEAS. Hence, the WICC propagates offshore slowly enough in the NEAS to permit an analysis of the role of advection by considering the spatio-temporal variability along the 1000 m isobath; the model grid cells used in these figures are shown in Fig. 1.

A plot of the model variables along the 1000 m isobath (henceforth referred to as alongshore variation) shows that the WICC reverses at the end of October and the ML deepens uniformly poleward of ∼19.5°N during November (Fig. 9). This situation persists through December, except for the extreme north of the NEAS, i. e., on the continental slope off the southern coast of Pakistan, where the ML deepens more than in the rest of the NEAS. In January, the distinction between the northern and southern NEAS becomes more striking, with the ML deepening to over 130 m (less than 100 m) north (south) of ~22°N. The distinguishing latitude shifts poleward to ∼23°N and the alongshore gradient of MLD increases in February, when the ML shallows (deepens) to ∼60 m (∼140 m) in the southern (northern) NEAS. This north-south difference in MLD

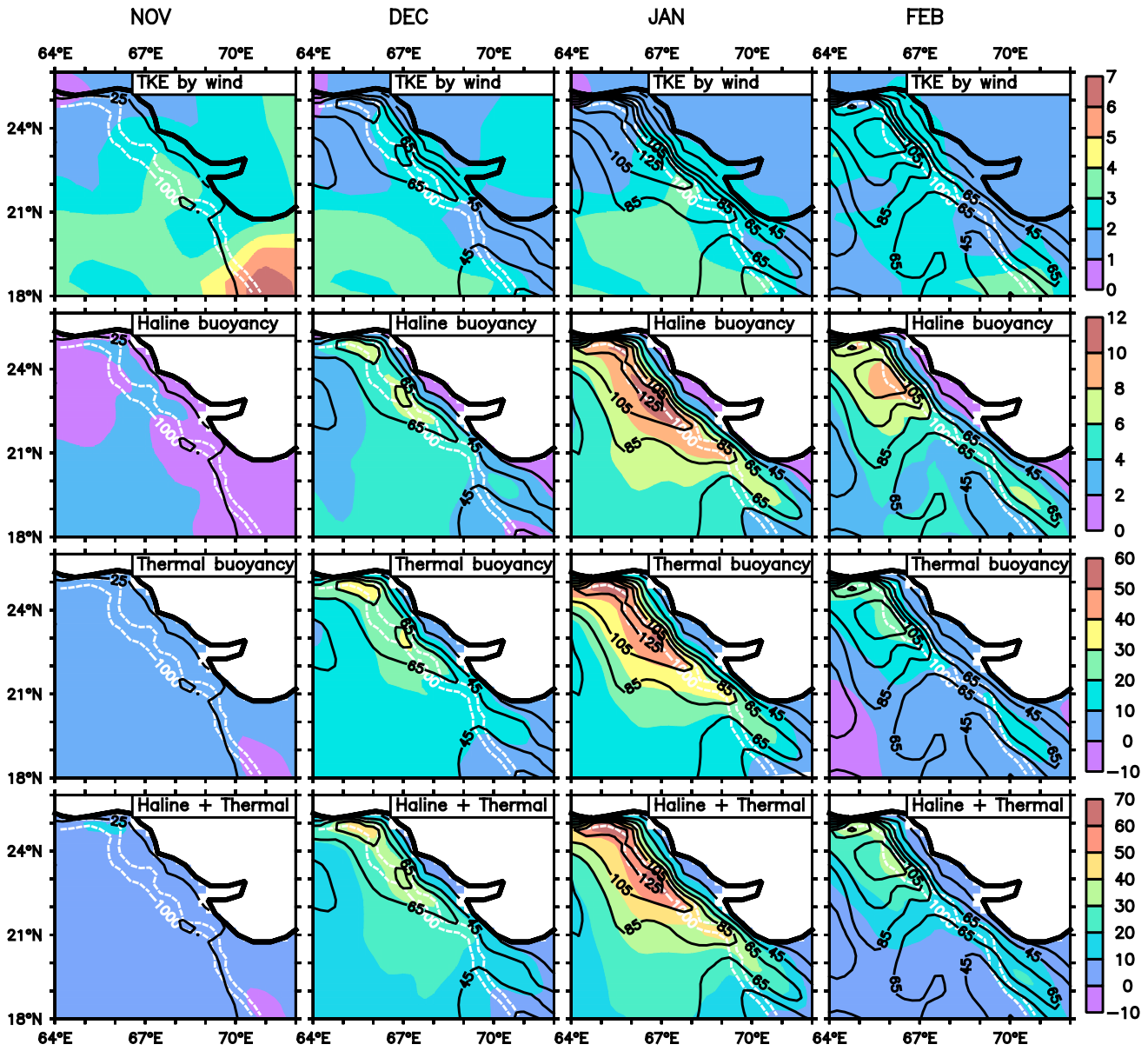


**Fig. 7** Monthly climatologies of the model turbulent kinetic energy due to the wind (*first row*), haline buoyancy flux (*second row*), thermal buoyancy flux (*third row*), and the total buoyancy flux (sum of haline and thermal buoyancy fluxes; *fourth row*) during November–February (from *left* to *right*). All these fields have units of $10^{-7}$ m$^3$ s$^{-3}$ (the values have been multiplied by $10^7$ before plotting). The daily buoyancy flux was averaged over the month to obtain the monthly climatology. Note that a positive buoyancy flux supports convective mixing and is therefore associated with a net heat flux out of the ocean (for thermal buoyancy flux) and an excess of evaporation over precipitation (for haline buoyancy flux). Overlaid on all panels is the MLD (m); the contour interval for MLD is 20 m. The 200 and 1000 m isobaths are marked

disappears in the second half of March as the ML shallows to almost 40 m all over the NEAS. This shallowing in March is a consequence of the increase in net shortwave flux (into the ocean), which overwhelms the latent-heat and longwave fluxes, leading to a classical detrainment (Kraus and Turner 1967; McCreary et al. 1996, 2009) situation.

The latitudinal dependence of SST becomes evident in December (Fig. 9). Note that the SST contours in the figure are almost flat from mid-December (mid-January) to the end of February in the southern (northern) NEAS, implying that SST barely changes even as the ML shallows (deepens) in February in the southern (northern) NEAS. The variation of SSS is in contrast to that of SST: except for the regime north of ∼24°N, where the SSS is relatively constant through November–March, it decreases almost monotonically through December–February and the lower

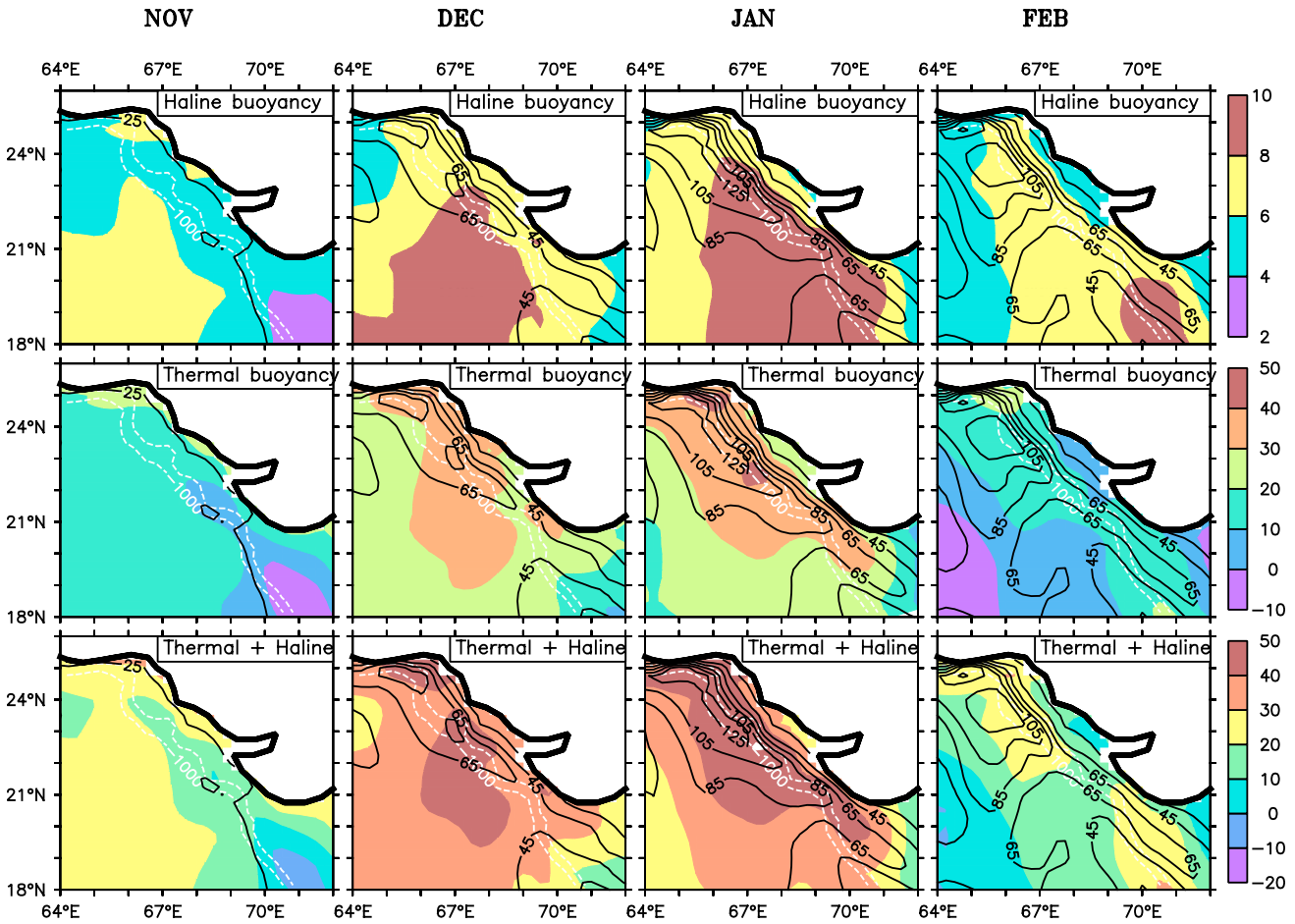


**Fig. 8** Monthly climatologies of the model depth-averaged buoyancy fluxes ($10^{-9}$ m$^2$ s$^{-3}$; all values have been multiplied by $10^9$ before plotting). Haline buoyancy flux (*top row*), depth-averaged thermal buoyancy flux (*middle row*), and the sum of these two depth-averaged buoyancy fluxes (*bottom row*) are shown for November–February (from *left* to *right*). The daily buoyancy flux was averaged over the month to obtain the monthly climatology. Overlaid on all panels is the MLD (m); the contour interval for MLD is 20 m. Note the striking difference between the patterns of these depth-averaged buoyancy fluxes and the buoyancy fluxes shown in Fig. 7: the depth-averaged fluxes change over a broader region, reflecting the larger scale associated with the changes due to the march of the season, and their pattern does not match that of the MLD. The 200 and 1000 m isobaths are marked

salinities extend farther poleward with time. There is a striking match between the variation of MLD (100–110 m contours) and SSS (36.10 psu contour), suggesting that it is the decrease in SSS, rather than a change in SST, that leads to the rapid shallowing of the ML south of ∼23°N during February.

The role of the WICC in decreasing the salinity along the continental slope is evident in an analysis of the salt budget for the ML (Fig. 10). Atmospheric forcing tends to increase salinity because evaporation exceeds precipitation, but it is more than compensated by the freshening due to the advection of waters of lower salinity from the south. Except for a few bursts (these intraseasonal bursts have a time scale of the order of a week) during November and February–March, the sub-surface processes (essentially entrainment and vertical advection; figure not shown) make but a meagre contribution to the salt budget of the ML. Hence, the ML shallows in the southern NEAS owing to the inflow of lower-salinity waters from the south.

A similar analysis of the heat budget of the ML (Fig. 11) shows a dominance of atmospheric forcing, with the significant contribution of horizontal advection restricted equatorward of 19°N till the end of January. The shortwave flux is dominated by a seasonal cycle, but the latent-heat and longwave fluxes exhibit intraseasonal bursts (Fig. 12). As with the salt budget, the sub-surface processes have a small effect on the ML temperature because the contributions of vertical advection and entrainment mixing tend to cancel throughout the winter monsoon (Fig. 13). Vertical advection tends to warm, rather than cool, the mixed layer because the vertical velocity is negative, i.e., downwelling-favourable. An

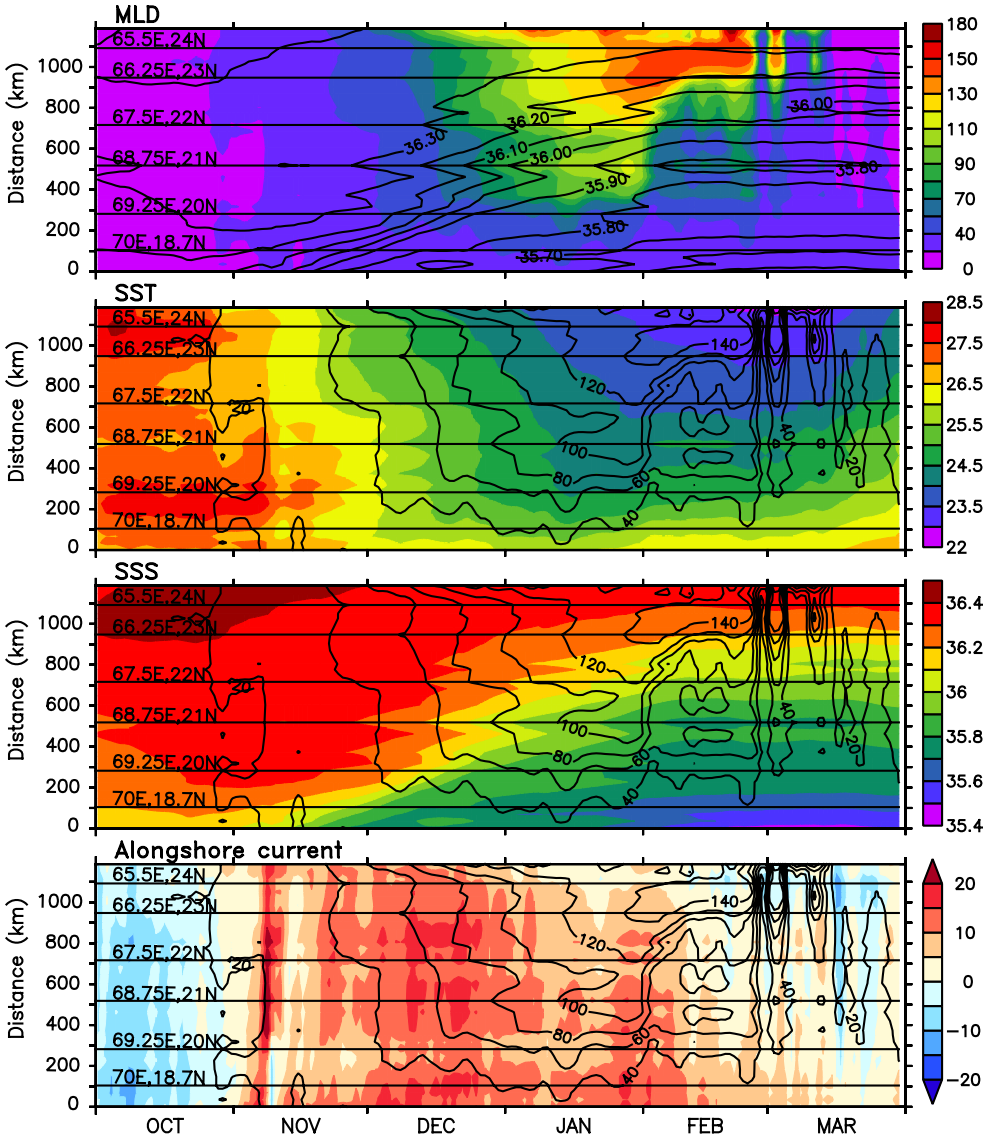


**Fig. 9** Variation during October–March of the model MLD (m, *top panel*), SST (°C, *second panel*), SSS (psu, *third panel*), and alongshore current (cm $s^{-1}$, *bottom panel*; positive poleward) along the 1000 m isobath. The model grid cells used for these plots are marked in Fig. 1. The abscissa is time and the ordinate gives the distance (in hundreds of kilometres) poleward along the 1000 m isobath from 18°N. The latitude and longitude are marked by *horizontal lines*. SSS contours are overlaid on the MLD panel and MLD contours are overlaid on the other three panels

exception is a relatively strong warming burst due to vertical advection at the end of October.

Though the WICC advects low-salinity waters poleward into the northern NEAS as well, the ML remains deep till the end of February because it deepens to over 100 m before the inflow of low-salinity water can decrease the ML salinity (Fig. 9). The buoyancy fluxes and the TKE due to the wind are sufficient (Fig. 14) to maintain the MLD at over 100 m until the shortwave radiation increases and latent-heat flux decreases in March (Fig. 12), enabling the ML to detrain and shallow to a depth of ∼40 m by the end of the month (Fig. 9).

The role of vertical advection, which tends to warm the ML because of downwelling, has largely been ignored in the literature. The downwelling in the NEAS, primarily forced by remote winds through the poleward propagation of Kelvin waves that lower the thermocline and raise sea level along the west coast of India during the winter monsoon (McCreary et al. 1993; Shankar and Shetye 1997; Shankar 1998, 2000; Shankar et al. 2002), counters the cooling due to entrainment of cooler, sub-surface waters. A consequence of these contrasting influences is that SST, or the ML temperature, is almost constant through January–February even as the ML shallows owing to the poleward advection of low-salinity

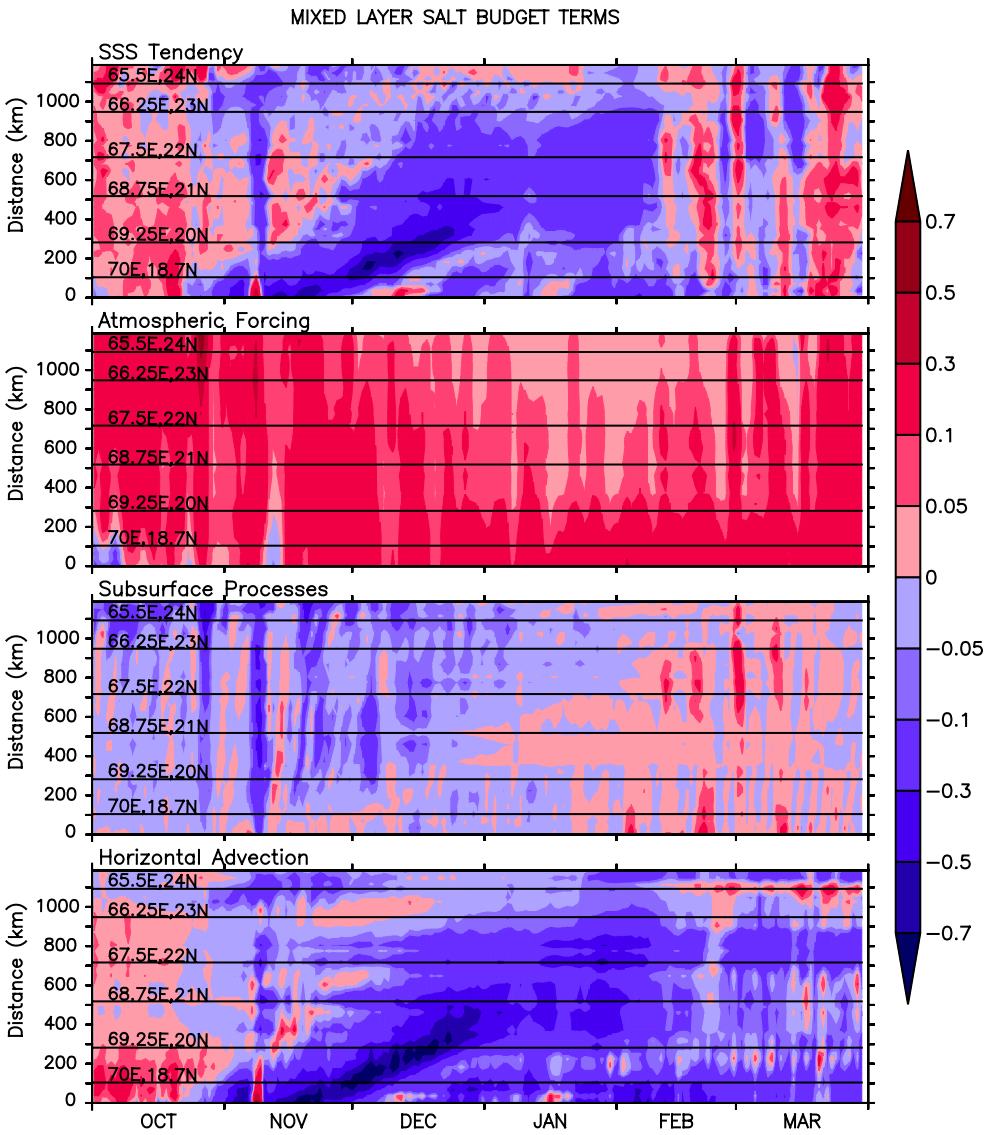


**Fig. 10** The ML salt budget during October–March. The tendency term (*top panel*) and the contributions of atmospheric forcing (*second panel*), sub-surface processes (*third panel*), and horizontal advection (*bottom panel*) are plotted along the 1000 m isobath. The unit is psu month$^{-1}$ and the model grid cells used for these plots are marked in Fig. 1. The sub-surface processes comprise vertical advection, entrainment, and turbulent processes (Vialard and Delecluse 1998; Kurian and Vinayachandran 2007). The abscissa is time and the ordinate gives the distance (in hundreds of kilometres) poleward from 18°N; the latitude and longitude are marked by *horizontal lines*

waters by the WICC. The inflow of low-salinity water at the surface increases the vertical salinity gradient at the base of the mixed layer (Fig. 15): the gradient, which was negative because of the Arabian Sea Salinity Minimum underlying the ASHSW in the ML (Shenoi et al. 1993) before November, turns positive as the ML shallows south of 23°N in January–February. As a result of this intrusion of low-salinity water at the surface, a weak barrier layer (Lukas and Lindström 1991; Vialard and Delecluse 1998) forms and the vertical temperature gradient weakens to near-zero values at the base of the mixed layer (Fig. 15). Therefore, the SST does not decrease in the southern NEAS in spite of the net heat flux being out of the ocean (Fig. 6) and the positive buoyancy fluxes (Fig. 14) therefore tending to deepen the ML. That the flux is still out of the ocean in February permits a balance between the cooling by air-sea fluxes and the warming due to the inflow of warmer water. Therefore, the SST remains almost constant even as the ML shallows by ∼50 m from January to February.

## 5 Discussion

In summary, we have used an OGCM to investigate the climatological spatio-temporal variability of the depth of the

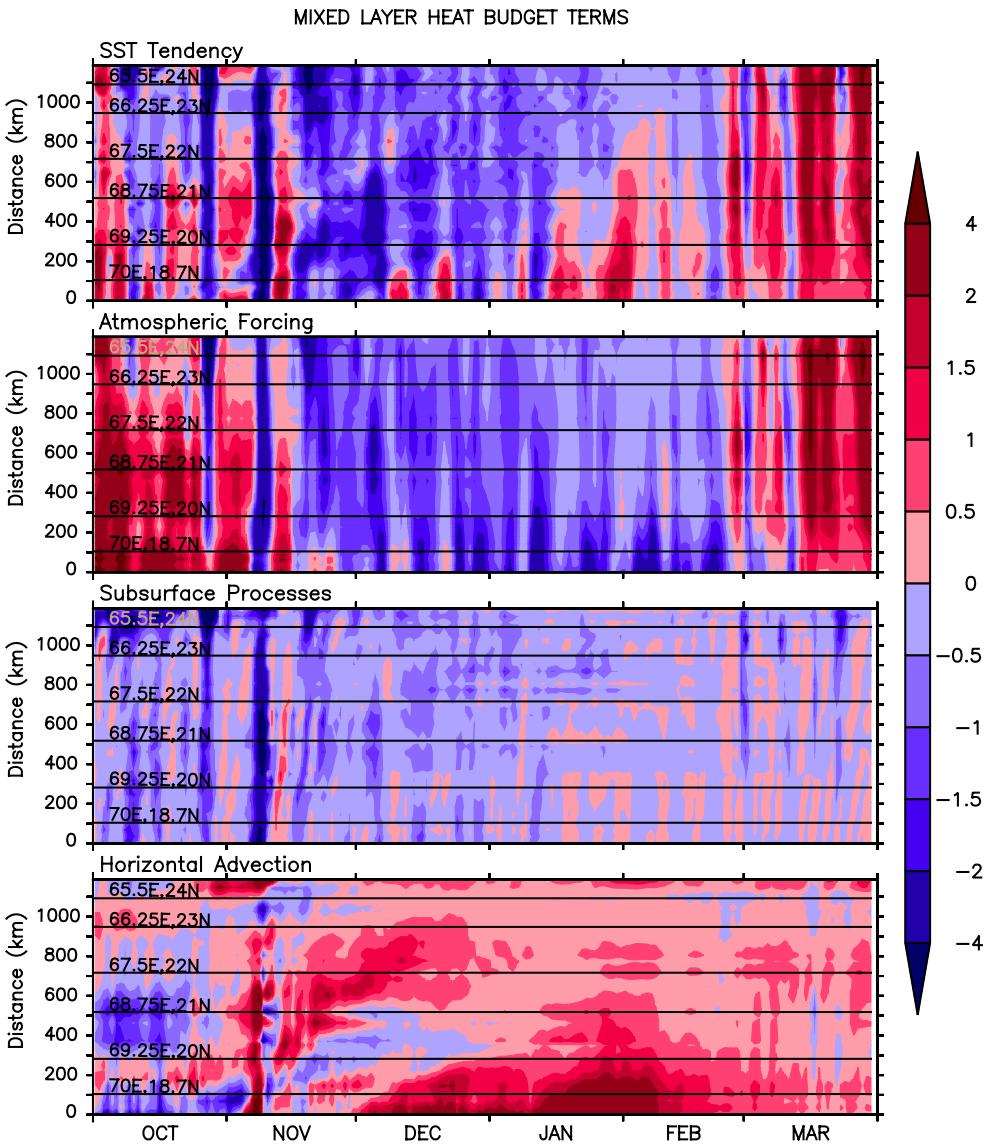


**Fig. 11** The ML heat budget during October–March. The tendency term (*top panel*) and the contributions of atmospheric forcing (*second panel*), sub-surface processes (*third panel*), and horizontal advection (*bottom panel*) are plotted along the 1000 m isobath. The unit is °C month$^{-1}$ and the model grid cells used for these plots are marked in Fig. 1. The sub-surface processes comprise vertical advection, entrainment, and turbulent processes (Vialard and Delecluse 1998; Kurian and Vinayachandran 2007). The abscissa is time and the ordinate gives the distance (in hundreds of kilometres) poleward from 18°N; the latitude and longitude are marked by *horizontal lines*

mixed layer in the NEAS during the winter monsoon. A description of this variability led to three questions.

The first question was the cause of the shallowing of the ML during January–February in the southern NEAS even as it continued to deepen in the north (Figs. 5, 9). Earlier hypotheses suggested that this difference between the northern and southern NEAS was due to the poleward advection of warmer, fresher waters by the WICC (Naqvi et al. 2006). Our simulations show that it is the salinity that is important: the alongshore salinity gradient in the eastern Arabian Sea, a consequence of the freshening in the south and excess of evaporation over precipitation in the north (Shetye et al. 1991a; Levitus 1982; Han et al. 2001; Antonov et al. 2010; Chatterjee et al. 2012) implies that the poleward WICC stabilises the water column (Fig. 15). In contrast to this freshening of the ML, its temperature, or the SST, barely changes during December–February, ruling out a similar impact due to the advection of warmer waters from the south.

The second question concerned the processes that led to the ML remaining deep in the northern NEAS in spite of the poleward advection of the low-salinity waters (Fig. 9). The simulations show that convective mixing deepens the ML in the northern NEAS before the waters of lower salinity reach this region. This fresher water from the south mixes with

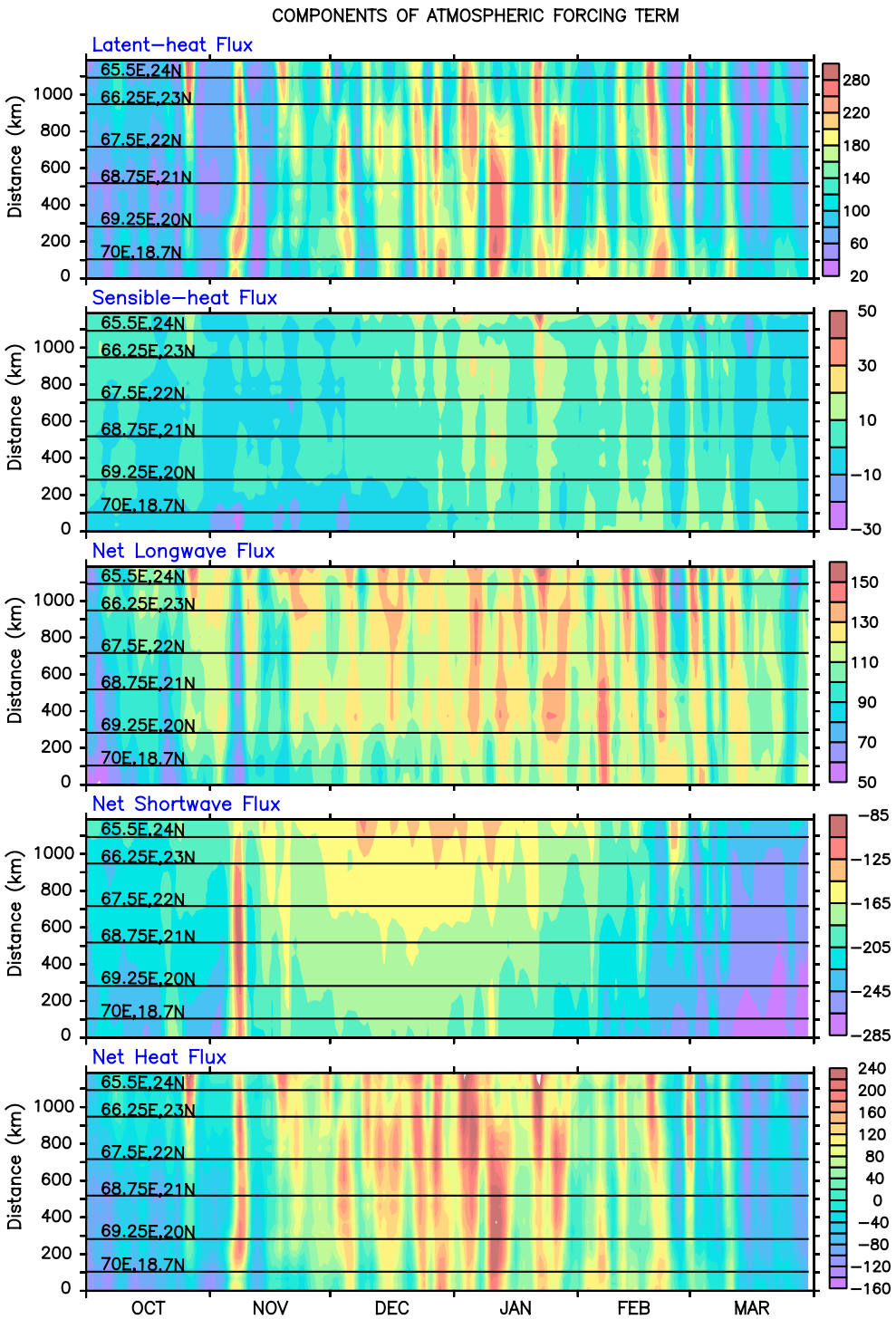


**Fig. 12** Contribution of components of the atmospheric-forcing term to the ML heat budget during October–March. The latent-heat flux (*top panel*), sensible-heat flux (*second panel*), net longwave flux (*third panel*), net shortwave flux (*fourth panel*), and net heat flux (*bottom panel*) are plotted along the 1000 m isobath. The unit is °C month$^{-1}$ and the model grid cells used for these plots are marked in Fig. 1. Note that the colour scale is different for each term. The abscissa is time and the ordinate gives the distance (in hundreds of kilometres) poleward from 18°N; the latitude and longitude are marked by *horizontal lines*

the high-salinity NASHSW to ensure that salinity does not increase in this part of the NEAS in spite of the evaporation. The deep mixed layer survives in the northern NEAS as the wind stirring and convective overturning generate sufficient turbulent energy for the ML to maintain the depth attained in January.

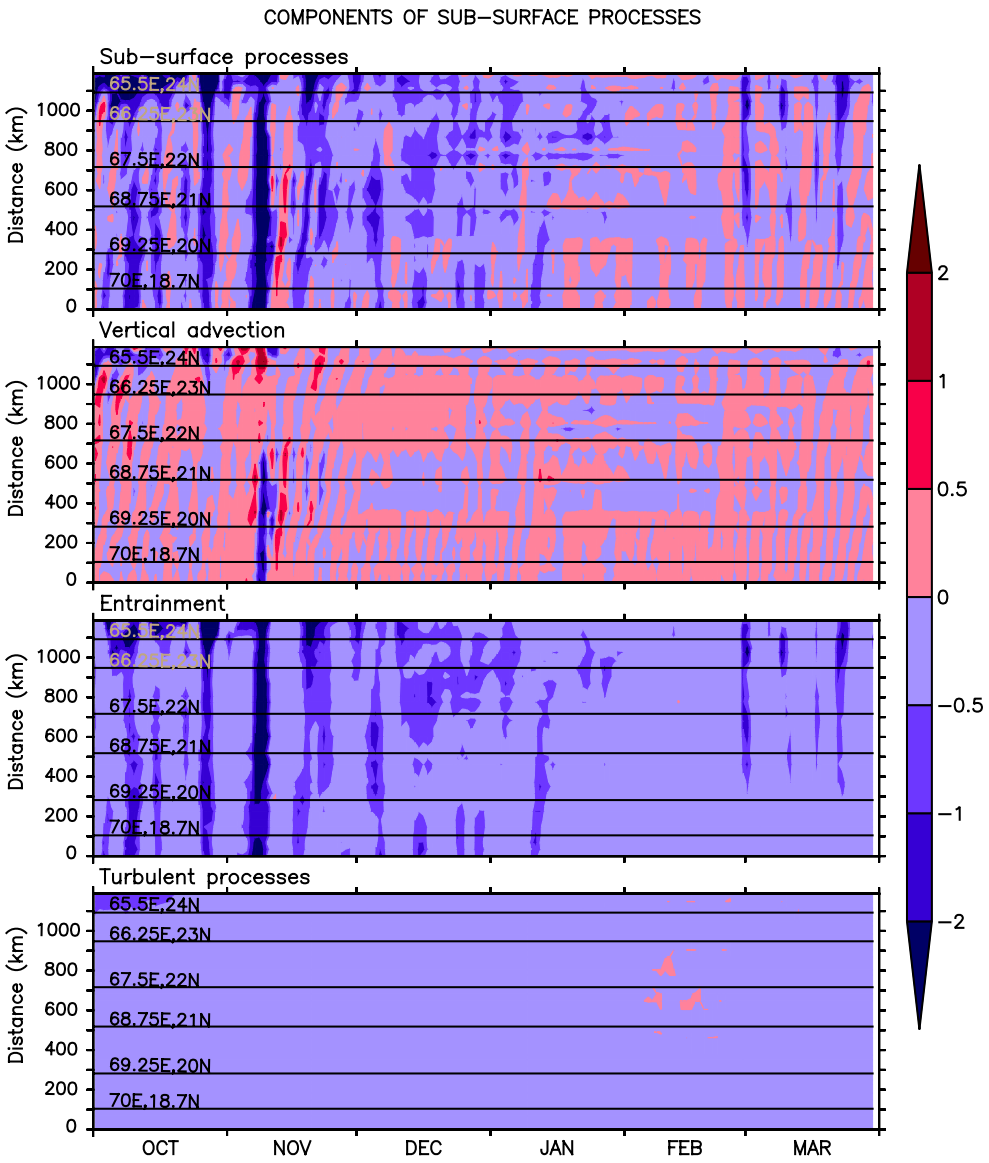


**Fig. 13** Contribution of components of the sub-surface processes to the ML heat budget during October–March. The sub-surface processes term (*top panel*) is plotted along the 1000 m isobath along with its components: vertical advection (*second panel*), entrainment (*third panel*), and turbulent processes (*bottom panel*). The unit is °C month$^{-1}$ and the model grid cells used for these plots are marked in Fig. 1. The abscissa is time and the ordinate gives the distance (in hundreds of kilometres) poleward from 18°N; the latitude and longitude are marked by *horizontal lines*

The third question concerned the SST: why is it almost constant even though the MLD changes by over 50 m during December–February in the southern NEAS (Fig. 9)? Our simulations show that the atmospheric fluxes tend to cool the ML, but this cooling is countered by the warming due to horizontal advection (Fig. 11). An important process is downwelling, which tends to warm the ML, almost cancelling the cooling due to entrainment mixing that continues even as the ML shallows in the southern NEAS (Fig. 13). This balance leads to the formation of a weak barrier layer below the ML in the southern NEAS (Fig. 15), precluding cooling by entrainment.

This spatio-temporal difference in the evolution of SST and MLD in the NEAS implies that the former, which is measurable from space, cannot be used as a proxy for the latter, for which one has to rely on the sparse and sporadic data available from Argo floats. It is now possible to measure salinity from space, but the variation in salinity in the NEAS is of the order of 0.5 psu, currently beyond the measurement accuracy (∼2 psu) of the Aquarius salinity sensor (Tsontos 2014) and of the same order as that of the SMOS (Soil Moisture and Ocean Salinity) sensor (∼0.36 psu; Ratheesh et al. 2012; Subrahmanyam et al.

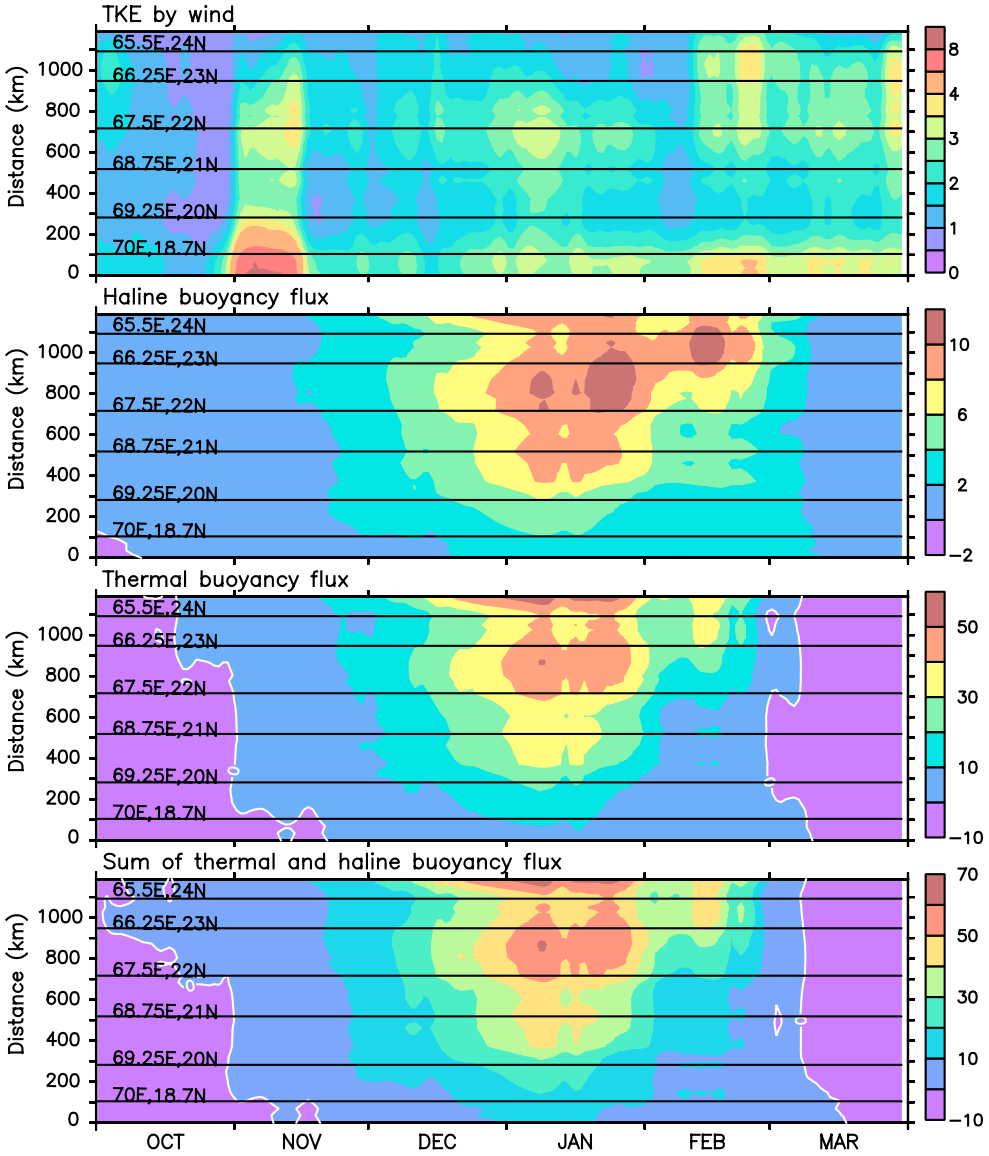


**Fig. 14** The turbulent kinetic energy input by the wind (*top panel*), haline buoyancy flux (*second panel*), thermal buoyancy flux (*third panel*), and the sum of thermal and haline buoyancy fluxes (*bottom panel*) along the 1000 m isobath during October–March. The unit is $10^{-7}$ m$^3$ s$^{-3}$ (the values have been multiplied by $10^7$ before plotting) and the model grid cells used for these plots are marked in Fig. 1. The thermal and haline buoyancy fluxes were smoothed with a 15-day running mean to damp the noise in the daily fields. The abscissa is time and the ordinate gives the distance (in hundreds of kilometres) poleward from 18°N; the latitude and longitude are marked by *horizontal lines*

2013), ruling out the use of these sensors in this region until accuracies improve. The spatio-temporal changes in salinity in the NEAS during winter are much smaller than the changes seen in the northern Bay of Bengal (Wyrtki 1971; Shetye et al. 1991b, 1993, 1996; Chatterjee et al. 2012), but the physical processes, including the formation of a barrier layer, are the same. Even the much weaker salinity gradients in the NEAS play an important role in determining the MLD in the region.

The simulations show that SST and MLD in the NEAS respond but weakly to the intraseasonal bursts evident in the winds and air-sea radiative and heat fluxes (Figs. 9, 11, 12). More TKE is needed to sustain the deep MLs of the NEAS than for the much shallower MLs of the northern Bay of Bengal (Shetye et al. 1991b, 1996). These deeper MLs are less susceptible to the weaker intraseasonal perturbations in the winds, precluding a strong intraseasonal response of SST and MLD in the NEAS to the intraseasonal variability in the fluxes. This relative lack of intraseasonal variability in the SST and MLD in the NEAS is in striking contrast to what happens in the northern Bay of Bengal (Premkumar et al. 2000; Sengupta et al. 2001),

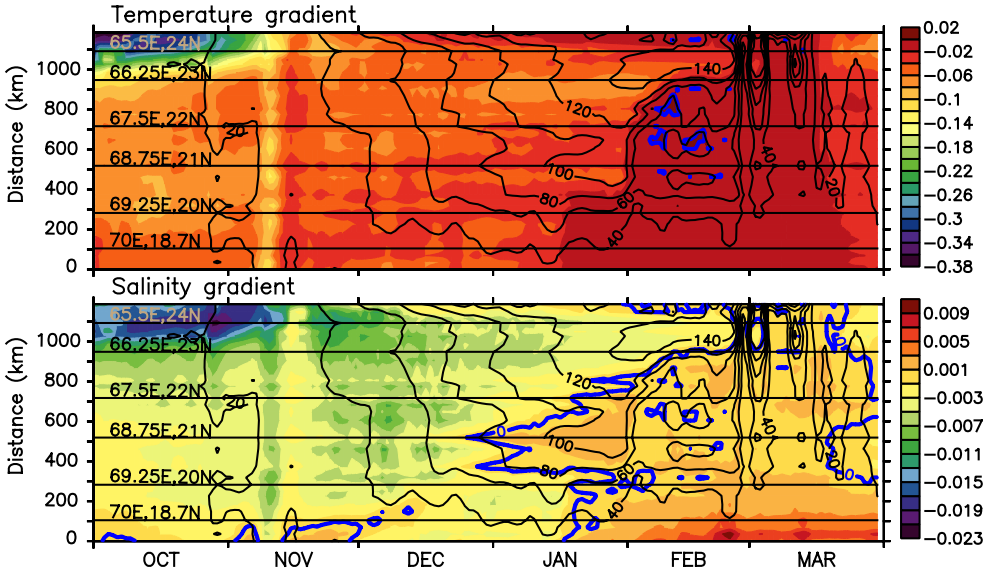


**Fig. 15** Temperature gradient (°C $m^{-1}$, *top panel*) and salinity gradient (psu $m^{-1}$, *bottom panel*) at the base of the ML along the 1000 m isobath during October–March. The model grid cells used for these plots are marked in Fig. 1. The abscissa is time and the ordinate gives the distance (in hundreds of kilometres) poleward from 18°N; the latitude and longitude are marked by *horizontal lines*. The zero contour is shown (*blue curve*) and the MLD (m) contours (*black curves*) are overlaid

where the shallow ML can respond rapidly to perturbations in the winds or air-sea heat and radiative fluxes.

The MLD in the NEAS is determined by an interplay of two very different physical processes. The convective mixing depends on the winds, radiative fluxes, SST, air temperature, and specific humidity, all of which are local to the region. For example, the relative weakness of the winds in the northern NEAS (Figs. 4, 6) can be attributed to the Makran Range that rises to a height of over 1000 m just north of the southern coast of Pakistan (Fig. 1). Farther south in the NEAS, the winds blow in from the flatter terrain of the plains of India and Pakistan (Fig. 1); these northeasterly winds are therefore stronger and lead to a higher latent-heat flux (Fig. 4). The other key process is advection by the WICC, whose seasonal cycle is not locally forced [as realised by Banse (1984) and Shetye and Shenoi (1988)], but has been shown to be primarily forced remotely from the east coast of India (McCreary et al. 1993; Shankar and Shetye 1997; Shankar et al. 2002), with the alongshore winds off southwest India also playing a role (Shetye et al. 2008; Amol et al. 2012, 2014). These two processes are not necessarily correlated, implying the possibility of considerable interannual variability in the evolution and extent of these deep mixed layers in the NEAS.

This role of horizontal advection in determining the spatio-temporal variability of the MLD in the NEAS during winter has implications for water-mass formation in the region. Two of the high-salinity water masses of the Arabian Sea, the Persian Gulf Water (PGW) mass and Red Sea Water (RSW) mass (Rochford 1964; Bower et al. 2000; Schott and McCreary 2001), form in semi-enclosed basins (the Persian Gulf and the Red Sea, respectively), and their region of formation is therefore limited. By inhibiting the formation of deep MLs in the southern NEAS, the WICC limits the region of formation of the ASHSW (Rochford 1964) and NASHSW (Banse and Postel 2009). Hence, even though these water masses form in the open ocean, their region of formation is also highly restricted. The poleward WICC also constrains the movement of the water upwelled off the Oman coast during the previous summer monsoon, forcing it to spread southward via the central Arabian Sea (Valsala 2009).

In conclusion, we have shown that advection by the WICC, and therefore ocean dynamics at the basin scale, plays a significant role in determining the MLD, and, by extension, the chlorophyll concentration and ecosystem dynamics, in the NEAS. Our results imply that the conventional approach of averaging over boxes (see Fig. 3 for an example of such averaging) for studying the impact of physics on biogeochemistry can mask important details that are due to advection because it is the advective component of any budget that is most affected by the averaging process. Changes in air-sea fluxes, in contrast, tend to occur over larger spatial scales and are less affected by the averaging.

Recent data from high-resolution CTD (conductivity–temperature–depth) sections across fronts and filaments in the NEAS show considerable variation in the chlorophyll and pigment concentration across these short-scale features (Vipin et al. 2015; Roy et al. 2015), which

too are a consequence of dynamics. These data suggest that the response of the ecosystem to the physical forcing may depend on when the front or filament forms during the winter monsoon, there being a difference between the fronts that form in November, when the convective mixing starts to deepen the ML in the NEAS, and the fronts that form in late January, when the ML reaches its maximum depth (Roy and Anil 2015). Therefore, the seasonal evolution of the ML in the NEAS during the winter monsoon has an impact even on processes that occur on a much smaller spatial scale and over a much shorter temporal scale. Our results show that this variation of the ML in the NEAS, which is a small, but productive, part of the Arabian Sea, is the result of a more complex interplay of physical processes than hitherto believed.

These results, which highlight the role of advection and salinity in determining the MLD and SST in the NEAS, have implications for the Indian summer monsoon as well (Raghu Murtugudde, personal communication 2015). Coupled-model studies show that the chlorophyll concentration during late spring (March) in the northern Arabian Sea has an impact on the model MLD, which, in turn, has an impact on the summer-monsoon precipitation (Turner et al. 2012). Coupled models also tend to exhibit a cold bias in the SST in the northern Arabian Sea and this cold bias tends to decrease the summer-monsoon precipitation (Levine and Turner 2011; Marathayil et al. 2013; Levine et al. 2013; Sandeep and Ajayamohan 2014). Our results suggest that it is important for the coupled models to simulate the salinity correctly because it has a significant influence on the spring MLD even though the variations in SSS in the NEAS are an order of magnitude smaller than in the northern Bay of Bengal, where the role of the surface low-salinity surface layer in keeping the bay warmer during the summer monsoon is better documented (see, for example, Shenoi et al. 2002).

**Acknowledgments** This study was funded by the OCEAN FINDER programme of CSIR-NIO. We thank S. R. Shetye for inspiring this programme, K. Banse for pointing (D. Shankar) to the need for the NEAS to be "looked at by young and fresh minds", A. C. Anil for several useful discussions on the ecosystem dynamics of the region, A. Mukherjee for his assistance with the model, and Amol Prakash for help with Ferret, which has been used extensively for analysis and graphics. Comments from Raghu Murtugudde, Theodore Durland, Dileep Kumar, and Kerala Varma on a preprint and the critical comments of two anonymous reviewers helped improve the manuscript. The model was run on the high-performance-computing (HPC) systems at CSIR-CMMACS and CSIR-NIO; the support provided by Ashalata Marandi and the staff handling these HPC systems is gratefully acknowledged. R. Remya acknowledges the Council of Scientific and Industrial Research (CSIR; for financial support) and AcSIR; P. N. Vinayachandran and A. Behera acknowledge funding from INCOIS under the HOOFS (High-resolution Operational Ocean Forecast and reanalysis System) programme. This is CSIR-NIO contribution 5822 and ESSO-INCOIS contribution 233.

## References

Adcroft A, Campin JM (2004) Rescaled height coordinates for accurate representation of free-surface flows in ocean circulation models. Ocean Model 7:269–284

Amol P, Shankar D, Aparna SG, Shenoi SSC, Fernando V, Mukherjee A, Agarvedekar Y, Khalap ST, Satelkar NP (2012) Observational evidence from direct current measurements for propagation of remotely forced waves on the shelf off the west coast of India. J Geophys Res 117:C05017. doi:10.1029/2011JC007606

Amol P, Shankar D, Fernando V, Mukherjee A, Aparna SG, Fernandes R, Michael GS, Khalap ST, Satelkar NP, Agarvedekar Y, Gaonkar MG, Tari AP, Kankonkar A, Vernekar SP (2014) Observed intraseasonal and seasonal variability of the West India Coastal Current on the continental slope. J Earth Syst Sci 123:1045–1074

Antonov JI, Seidov D, Boyer TP, Locarnini RA, Mishonov AV, Garcia HE (2010) World Ocean Atlas 2009, vol 2. Salinity. Noaa atlas nesdis 69, NOAA, U.S. Gov. Printing Office, Washington, DC

Banse K (1968) Hydrography of the Arabian Sea shelf of India and Pakistan and effects on demersal fishes. Deep Sea Res 15:45–79

Banse K (1984) Marine geology and oceanography of Arabian Sea and coastal Pakistan, Scientific and Academic Editions. Van Nostrand Reinhold Co., New York

Banse K (1987) Seasonality of phytoplankton chlorophyll in the central and northern Arabian Sea. Deep Sea Res 34:713–723

Banse K, Postel JR (2009) Wintertime convection and ventilation of the upper pycnocline in the northernmost Arabian Sea. Geophys Monogr Ser 185:87–117. doi:10.1029/2008GM000704

Bower A, Hunt HD, Price JF (2000) Character and dynamics of the Red Sea and Persian Gulf outflows. J Geophys Res 105:6387–6414

Bryan K, Lewis LJ (1979) A water mass model of the world ocean. J Geophys Res 84:2503–2517

Carruthers JN, Gogate SS, Naidu JR, Laevastu T (1959) Shorewards upslope of the layer of minimum oxygen off Bombay: it influence on marine biology, particularly fisheries. Nature 183:1084–1087

Chatterjee A, Shankar D, Shenoi SSC, Reddy GV, Michael GS, Ravichandran M, Gopalkrishna VV, Rao EPR, Bhaskar TVSU, Sanjeevan VN (2012) A new atlas of temperature and salinity for the North Indian Ocean. J Earth Syst Sci 121:559–593. doi:10.1007/s12040-012-0191-9

Chatterjee A, Shankar D, McCreary JP, Vinayachandran PN (2013) Yanai waves in the western equatorial Indian Ocean. J Geophys Res 118:1556–1570. doi:10.1002/jgrc.20121

Cronin MF, Sprintall J (2001) Wind and buoyancy-forced upper ocean. In: Steele JH, Turekian KK, Thorpe SA (eds) Encyclopedia of ocean science. Academic Press, Waltham. doi:10.1006/rwos.2001.0157

Gibson JK, Kallberg P, Uppala S, Hernandez A, Serrano ANE (1997) ECMWF reanalysis project report series: 1. ERA-15 description. Technical report, European Centre for Medium-Range Weather Forecasting

Gomes HR, Goes JI, Matondkar SGP, Buskey EJ, Basu S, Parab S, Thoppil P (2014) Massive outbreaks of *Noctiluca scintillans* blooms in the Arabian Sea due to spread of hypoxia. Nat Commun. doi:10.1038/ncomms5862

Griffies SM (2009) Elements of MOM4p1. GFDL ocean group. Technical report 6, NOAA/Geophysical Fluid Dynamics Laboratory. http://www.gfdl.noaa.gov/

Griffies SM, Hallberg RW (2000) Biharmonic friction with a Smagorinsky viscosity for use in large-scale eddy-permitting ocean models. Mon Weather Rev 128:2935–2946

Han W (1999) Influence of salinity on dynamics, thermodynamics and mixed-layer physics in the Indian Ocean. PhD thesis, Nova Southeastern University

Han W, McCreary JP, Kohler KE (2001) Influence of precipitation minus evaporation and Bay of Bengal rivers on dynamics, thermodynamics, and mixed layer physics in the upper Indian Ocean. J Geophys Res 106:6895–6916

Hood RR, Wiggert JD, Naqvi SWA (2009) Indian ocean research: opportunities and challenges. Geophys Monogr Ser 185:409–428. doi:10.1029/2008GM000714

Jackett DR, McDougall TJ, Feistel R, Wright DG, Griffies SM (2006) Algorithms for density, potential temperature, conservative temperature, and freezing temperature of seawater. J Atmos Ocean Technol 23:1709–1728

Koné V, Aumont O, Lévy M, Resplandy L (2009) Physical and biogeochemical controls of the phytoplankton seasonal cycle in the Indian Ocean: a modeling study. Geophys Monogr Ser 185:147–166. doi:10.1029/2008GM000700

Kraus EB, Turner JS (1967) A one-dimensional model of the seasonal thermocline. II: the general theory and its consequences. Tellus 119:98–106

Kurian J, Vinayachandran PN (2007) Mechanisms of formation of Arabian Sea mini warm pool in a high-resolution OGCM. J Geophys Res 112:C05009. doi:10.1029/2006JC003631

Large WG, McWilliams JC, Doney SC (1994) Oceanic vertical mixing: a review and a model with a nonlocal boundary layer parameterization. Rev Geophys 32:363–403

Levine RC, Turner AG (2011) Dependence of Indian monsoon rainfall on moisture fluxes across the Arabian Sea and the impact of coupled model sea surface temperature biases. Clim Dyn 38:2167–2190. doi:10.1007/s00382-011-1096-z

Levine RC, Turner AG, Marathayil D, Martin GM (2013) The role of northern Arabian Sea surface temperature biases in CMIP5 model simulations and future projections of Indian summer monsoon rainfall. Clim Dyn 41:155–172. doi:10.1007/s00382-012-1656-x

Levitus S (1982) Climatological atlas of the world ocean. NOAA professional paper 13, U.S. Government Printing Office, Washington, DC, 173 pp

Lévy M, Andre JM, Shankar D, Durand F, Shenoi SSC (2006) A quantitative method for describing the seasonal cycles of surface chlorophyll in the Indian Ocean. In: Frouin RJ, Agarwal VK, Kawamura H, Nayak S, Pan D (eds) Remote sensing of the marine environment, Proceedings of SPIE, vol 6406

Lévy M, Shankar D, Andre JM, Shenoi SSC, Durand F, Montégut CD (2007) Basin-wide seasonal evolution of the Indian Ocean's phytoplankton blooms. J Geophys Res 112:C12014. doi:10.1029/2007JC004090

Locarnini RA, Mishonov AV, Antonov JI, Boyer TP, Garcia HE (2010) World Ocean Atlas 2009, vol 1: temperature. Noaa atlas nesdis 68, NOAA, U.S. Gov. Printing Office, Washington, DC

Lukas RB, Lindström EJ (1991) The mixed layer of the western equatorial Pacific Ocean. J Geophys Res 96:3343–3357

Madhupratap M, Prasannakumar S, Bhattathiri PMA, Raghukumar S, Nair KKC, Ramaiah N (1996) Mechanism of biological response to winter cooling in the northeastern Arabian Sea. Nature 384:549–552

Marathayil D, Turner AG, Shaffrey LC, Levine RC (2013) Systematic winter sea-surface temperature biases in the northern Arabian Sea in HiGEM and the CMIP3 models. Environ Res Lett 8:014028. doi:10.1088/1748-9326/8/1/014028

Mariano AJ, Ryan EH, Perkins BD, Smithers S (1995) The Mariano global surface velocity analysis 1.0. Technical report USCG report CG-D-34-95, USCG

McCreary JP, Kundu PK, Molinary RL (1993) A numerical investigation of the dynamics, thermodynamics and mixed layer processes in the Indian Ocean. Prog Oceanogr 31:181–224

McCreary JP, Kohler KE, Hood RR, Olson DB (1996) A four-component ecosystem model of biological activity in the Arabian Sea. Prog Oceanogr 37:193–240

McCreary JP, Kohler KE, Hood RR, Smith S, Kindle J, Fischer AS, Weller RA (2001) Influences of diurnal and intraseasonal forcing on mixed-layer and biological variability in the central Arabian Sea. J Geophys Res 106:7139–7155

McCreary JP, Murtugudde R, Vialard J, Vinayachandran PN, Wiggert JD, Hood RR, Shankar D, Shetye S (2009) Biophysical processes in the Indian Ocean. Geophys Monogr Ser 185:9–32. doi:10.1029/2008GM000768

Monin AS, Obukhov AM (1954) Basic laws of turbulent mixing in the surface layer of the atmosphere. Contrib Geophys Inst Acad Sci USSR 24:163–187

Morel A, Antoine D (1994) Heating rate within the upper ocean in relation to its biooptical state. J Phys Oceanogr 24:1652–1665

Naqvi SWA (1991) Geographical extent of denitrification in the Arabian Sea in relation to some physical processes. Oceanol Acta 14:281–290

Naqvi SWA, Narvekar PV, Desa E (2006) Coastal biogeochemical processes in the north Indian Ocean. Coastal segment (14, S–W). In: Robinson AR, Brink KH (eds) The Sea, vol 14, chapter 19, Wiley, Hoboken, pp 723–781

Pankajakshan T, Ramaraju DV (1987) Intrusion of bay of bengal water into the Arabian sea along the west coast of india during northeast monsoon. In: Rao TSS, Natarajan R, Desai BN, Swami GN, Bhat SR (eds) Contributions in marine sciences. Dr. S. Z. Quasim Sastyabdapurthi felicitation volume. National Institute of Oceanography, Dona Paula, Goa, India, pp 237–244

Papa F, Durand F, Rossow WB, Rahman A, Bala S (2010) Satellite altimeter-derived monthly discharge of the Ganga–Brahmaputra river and its seasonal to interannual variations from 1993 to 2008. J Geophys Res 115:C12013. doi:10.1029/2009JC006075

Prasad TG, Ikeda M (2002a) A numerical study of the seasonal variability of Arabian Sea high-salinity water. J Geophys Res 107:3197. doi:10.1029/2001JC001139

Prasad TG, Ikeda M (2002b) The wintertime water mass formation in the northern Arabian Sea: a model study. J Phys Oceanogr 32:1028–1040

Prasannakumar S, Prasad TG (1996) Winter cooling in the northern Arabian Sea. Curr Sci 71:834–841

Prasannakumar S, Prasad TG (1999) Formation and spreading of Arabian Sea high-salinity water mass. J Geophys Res 104:1455–1464

Praveenkumar B, Vialard J, Lengaigne M, Murty VSN, McPhaden MJ (2012) TropFlux: air-sea fluxes for the global tropical oceans—description and evaluation. Clim Dyn 38:1521–1543. doi:10.1007/s00382-011-1115-0

Premkumar K, Ravichandran M, Kalsi SR, Sengupta D, Gadgil S (2000) First results from a new observational system over the Indian seas. Curr Sci 78:323–331

Qiu B, Kelly KA (1993) Upper-ocean heat balance in the Kuroshio extension region. J Phys Oceanogr 23:2027–2041

Rao SA, Gopalakrishna VV, Shetye SR, Yamagata T (2002) Why were cool SST anomalies absent in the Bay of Bengal during the 1997 Indian Ocean Dipole event? Geophys Res Lett 29:1555. doi:10.1029/2001GL014645

Ratheesh S, Mankad B, Basu S, Kumar R, Sharma R (2012) Assessment of satellite-derived sea-surface salinity in the Indian Ocean. IEEE Geosci Remote Sens Lett 10:428–431. doi:10.1109/LGRS.2012.2207943

Rochford DJ (1964) Salinity maxima in the upper 1000 m of the north Indian Ocean. Aust J Mar Freshw Res 15:1–24

Röske F (2001) An atlas of surface fluxes based on the ECMWF Reanalysis—a climatological data set to force global ocean general circulation models. Technical report 323, Max-Planck Institüt für Meteorologie, Hamburg, Germany

Roy R, Anil AC (2015) Complex interplay of physical forcing and *Prochlorococcus* population in ocean. Oceanography. doi:10.1016/j.pocean.2015.06.010

Roy R, Chithari R, Kulkarni V, Krishna MS, Sarma VVSS, Anil AC (2015) CHEMTAX-derived phytoplankton community structure associated with temperature fronts in the northeastern Arabian Sea. J Mar Syst 144:81–91. doi:10.1016/j.jmarsys.2014.11.009

Sandeep S, Ajayamohan RS (2014) Origin of cold bias over the Arabian Sea in climate models. Sci Rep 4. doi:10.1038/srep06403

Schott FA, McCreary JP (2001) The monsoon circulation of the Indian Ocean. Prog Oceanogr 51:1–123

Sengupta D, Goswami BN, Senan R (2001) Coherent intraseasonal oscillation of ocean and atmosphere during the Asian summer monsoon. Geophys Res Lett 28:4127–4130

Shankar D (1998) Low-frequency variability of sea level along the coast of India. PhD thesis, Goa University, Goa, India

Shankar D (2000) Seasonal cycle of sea level and currents along the coast of India. Curr Sci 78:279–288

Shankar D, Shetye SR (1997) On the dynamics of the Lakshadweep high and low in the southeastern Arabian Sea. J Geophys Res 102:12,551–12,562

Shankar D, Vinayachandran P, Unnikrishnan AS (2002) The monsoon currents in the north Indian Ocean. Prog Oceanogr 52:63–120

Shankar D, Gopalakrishna VV, Shenoi SSC, Durand F, Shetye SR, Rajan CK, Johnson Z, Araligidad N, Michael GS (2004) Observational evidence for westward propagation of temperature inversions in the southeastern Arabian Sea. Geophys Res Lett 31:L08305. doi:10.1029/2004GL019652

Shankar D, Aparna SG, McCreary JP, Suresh I, Neetu S, Durand F, Shenoi SSC, Saafani MAA (2010) Minima of interannual sea-level variability in the Indian Ocean. Prog Oceanogr 84(3–4):225–241. doi:10.1016/j.pocean.2009.10.002

Sharma GS (1968) Seasonal variation of some hydrographic properties of the shelf waters off the west coast of India. Bull Nat Inst Sci India 38:263–276

Shenoi SSC, Shetye SR, Gouveia AD, Michael GS (1993) Salinity extrema in the Arabian Sea. In: Ittekot V, Nair RR (eds) Monsoon biogeochemistry, Mitteilungen aus dem Geologisch-Paläontologischen Institut der Universität Hamburg, vol 76, SCOPE/UNEP Sonderband, pp 37–49

Shenoi SSC, Shankar D, Shetye SR (2002) Differences in heat budgets of the near-surface Arabian Sea and Bay of Bengal: implications for the summer monsoon. J Geophys Res 107. doi:10.1029/2000JC000679

Shenoi SSC, Shankar D, Shetye SR (2004) Remote forcing annihilates barrier layer in southeastern Arabian Sea. Geophys Res Lett L05307. doi:10.1029/2003GL019270

Shetye SR, Almeida AM (1985) An examination of the factors that influence the monthly-mean sea level along the coast of India. In: IOC/Unesco workshop on regional co-operation in marine science in the central Indian ocean and adjacent seas and gulfs, Colombo, Sri Lanka, IOC workshop reports, vol 37, pp 87–104

Shetye SR, Gouveia AD (1998) Coastal circulation in the north Indian Ocean. Coastal segment (14, S–W). In: Robinson AR, Brink KH (eds) The Sea, vol 11, chapter 18, Wiley, Hoboken, pp 523–556

Shetye SR, Shenoi SSC (1988) Seasonal cycle of surface circulation in the coastal north Indian Ocean. Proc Indian Acad Sci 97:53–62

Shetye SR, Gouveia AD, Shenoi SSC, Sundar D, Michael GS, Almeida AM, Santanam K (1990) Hydrography and circulation off the west coast of India during the southwest monsoon 1987. J Mar Res 48:359–378

Shetye SR, Gouveia AD, Shenoi SSC, Michael GS, Sundar D, Almeida AM, Santanam K (1991a) The coastal current off western India during the northeast monsoon. Deep Sea Res 38:1517–1529

Shetye SR, Shenoi SSC, Gouveia AD, Michael GS, Sundar D, Nampoothiri G (1991b) Wind-driven coastal upwelling along the western boundary of the Bay of Bengal during the southwest monsoon. Cont Shelf Res 11:1397–1408

Shetye SR, Gouveia AD, Shenoi SSC (1992) Does winter cooling lead to the subsurface salinity minimum off Saurashtra, India. In: Desai BN (ed) Oceanography of the Indian Ocean. Oxford and India Book House, Calcutta, pp 617–625

Shetye SR, Gouveia AD, Shenoi SSC, Sundar D, Michael GS, Nampoothiri G (1993) The western boundary current of the seasonal subtropical gyre in the Bay of Bengal. J Geophys Res 98:945–954

Shetye SR, Gouveia AD, Shankar D, Shenoi SSC, Vinayachandran PN, Sundar D, Michael GS, Nampoothiri G (1996) Hydrography and circulation in the western Bay of Bengal during the northeast monsoon. J Geophys Res 101:14,011–14,025

Shetye SR, Suresh I, Shankar D, Sundar D, Jayakumar S, Mehra P, Prabhudesai RG, Pednekar PS (2008) Observational evidence for remote forcing of the West India Coastal Current. J Geophys Res 113:C11001. doi:10.1029/2008JC004874

Sindhu B, Suresh I, Unnikrishnan AS, Bhatkar NV, Neetu S, Michael GS (2007) Improved bathymetric datasets for the shallow water regions in the Indian Ocean. J Earth Syst Sci 116:261–274

Stacey MW, Pond S, Nowak ZP (1995) A numerical model of the circulation in Knight Inlet, British Columbia, Canada. J Phys Oceanogr 25:1037–1062

Subrahmanyam B, Grunseich G, Nyadjro ES (2013) Preliminary SMOS salinity measurements and validation in the Indian Ocean. IEEE Trans Geosci Remote Sens 51:19–27. doi:10.1109/TGRS.2012.2199122

Sweeney C, Gnanadesikan A, Griffies SM, Harrison MJ, Rosati AJ, Samuels BL (2005) Impacts of shortwave penetration depth on large-scale ocean circulation and heat transport. J Phys Oceanogr 35:1103–1119. doi:10.1175/JPO2740.1

Tsontos V (2014) Aquarius user guide: aquarius dataset version 3.0, guide version 6.0, JPL-D-70012, AQ-010-UG-0008. Physical Oceanography Distributed Active Archive Center (PO.DAAC), Jet Propulsion Laboratory, Pasadena, California, USA

Turner AG, Joshi M, Robertson ES, Woolnough SJ (2012) The effect of Arabian Sea optical properties on SST biases and the South Asian summer monsoon in a coupled GCM. Clim Dyn 39:811–826. doi:10.1007/s00382-011-1254-3

Valsala V (2009) Different spreading of Somali and Arabian coastal upwelled waters in the northern Indian Ocean: a case study. J Oceanogr 65:803–816

Varma KK, Das VK, Gouveia AD (1980) Thermohaline structure and watermasses in the northern Arabian Sea during February–April. Indian J Mar Sci 9:148–155

Vialard J, Delecluse P (1998) An OGCM study for the TOGA decade. Part II: Barrier-layer formation and variability. J Phys Oceanogr 28:1089–1106

Vinayachandran PN, Kurian J, Neema CP (2007) Indian Ocean response to anomalous conditions during 2006. Geophys Res Lett 34. doi:10.1029/2007GL030194

Vipin P, Sarkar K, Aparna SG, Shankar D, Sarma VVSS, Gracias DG, Krishna MS, Srikanth G, Mandal R, Rao EPR, Rao NS (2015) Evolution and sub-surface characteristics of an SST filament and front in the northeastern Arabian Sea during November–December 2012. J Mar Syst 150. doi:10.1016/j.jmarsys.2015.05.003

Vörösmarty CJ, Fekete B, Tucker BA (1996) River discharge database, version 1.0 (RivDIS v1.0), vols 0–6, a contribution to IHP-V Theme 1, technical documents in hydrology series. Technical report, UNESCO, Paris

Wiggert JD, Jones BH, Hickey TD, Weller RA, Brink KH, Marra J, Codispoti LA (2000) The northeast monsoon's impact on

mixing, phytoplankton biomass and nutrient cycling in the Arabian Sea. Deep Sea Res Part II 47:1353–1385

Wiggert JD, Murtugudde RG, McClain CR (2002) Processes controlling interannual variations in wintertime (northeast monsoon) biomass in the central Arabian Sea. Deep Sea Res Part II 49:2319–2343

Wiggert JD, Hood RR, Banse K, Kindle JC (2005) Monsoon-driven biogeochemical processes in the Arabian Sea. Prog Oceanogr 65:176–213

Wiggert JD, Murtugudde RG, Christian JR (2006) Annual ecosystem variability in the tropical Indian Ocean: results of a coupled biophysical ocean general circulation model. Deep Sea Res Part II 53:644–676

Wiggert JD, Vialard J, Behrenfeld MJ (2009) Basin-wide modification of dynamical and biogeochemical processes by the positive phase of the Indian Ocean dipole during the SeaWiFS era. Geophys Monogr Ser 185:385–407. doi:10.1029/2008GM000776

Wyrtki K (1971) Oceanographic atlas of the international Indian ocean expedition. National Science Foundation, Washington, DC, 531 pp

Xie P, Arkin PA (1997) Global precipitation: a 17-year monthly analysis based on gauge observations, satellite estimates, and numerical model outputs. Bull Am Meteorol Soc 78:2539–2558